© 2024. Published by The Company of Biologists Ltd | Development (2024) 151, dev202128. doi:10.1242/dev.202128

RESEARCH ARTICLE

# Long-range formation of the Bicoid gradient requires multiple dynamic modes that spatially vary across the embryo

**Thamarailingam Athilingam[1,2], Ashwin V. S. Nelanuthala[3], Catriona Breen[4,*], Narain Karedla[5], Marco Fritzsche[5], Thorsten Wohland[3,6,‡] and Timothy E. Saunders[1,2,3,‡]**

## ABSTRACT

Morphogen gradients provide essential positional information to gene networks through their spatially heterogeneous distribution, yet how they form is still hotly contested, with multiple models proposed for different systems. Here, we focus on the transcription factor Bicoid (Bcd), a morphogen that forms an exponential gradient across the anterior-posterior (AP) axis of the early *Drosophila* embryo. Using fluorescence correlation spectroscopy we find there are spatial differences in Bcd diffusivity along the AP axis, with Bcd diffusing more rapidly in the posterior. We establish that such spatially varying differences in Bcd dynamics are sufficient to explain how Bcd can have a steep exponential gradient in the anterior half of the embryo and yet still have an observable fraction of Bcd near the posterior pole. In the nucleus, we demonstrate that Bcd dynamics are impacted by binding to DNA. Addition of the Bcd homeodomain to eGFP::NLS qualitatively replicates the Bcd concentration profile, suggesting this domain regulates Bcd dynamics. Our results reveal how a long-range gradient can form while retaining a steep profile through much of its range.

**KEY WORDS: Fluorescence correlation spectroscopy, Bicoid, *Drosophila* embryo, Morphogens, Diffusion**

## INTRODUCTION

Morphogens are molecules that provide crucial spatial and temporal information to cells during development (Briscoe and Small, 2015; Wartlick et al., 2009). Knowing how morphogen gradients form and on what time scales is essential for understanding how information can be precisely decoded (Gregor et al., 2007b; Huang et al., 2017; Kicheva et al., 2007; Yu et al., 2009). Despite intensive study, the underlying dynamics of morphogen gradient formation remain controversial (Huang and Saunders, 2020; Kerszberg and Wolpert, 1998; Kornberg, 2014; Stapornwongkul and Vincent, 2021). A longstanding model is that morphogen gradients are formed by localised synthesis and diffusive processes combined with protein degradation or trapping (the SDD model) (Driever and Nüsslein-Volhard, 1988; Gregor et al., 2007b; Grimm et al., 2010; Yu et al., 2009). Even for systems that appear to be driven by diffusion, the SDD model is only an approximation and often requires adaption to system specifics (Gregor et al., 2007b; Yu et al., 2009).

Alternative hypotheses for generating a long-range gradient include distributed sources of morphogen (Ali-Murthy and Kornberg, 2016; Spirov et al., 2009) and long-range transport via cytonemes (Roy et al., 2014; Stanganello et al., 2015). For example, competing models have been proposed to explain whether Decapentaplegic forms through long-range diffusion, cytoneme-mediated transport or endocytic recycling (Romanova-Michaelides et al., 2022; Roy et al., 2014; Zhou et al., 2012). The shape of the morphogen profile can be adjusted by the mode of degradation (Eldar et al., 2003; Müller et al., 2013; Yu et al., 2009), which may make the gradient more robust to variation in morphogen protein levels (Eldar et al., 2003; He et al., 2010; Saunders and Howard, 2009). The morphogen profile can also be modulated through receptor binding (Stapornwongkul and Vincent, 2021; Veerapathiran et al., 2020).

A range of quantitative techniques have been used to measure morphogen dynamics *in vivo*. These include fluorescence correlation spectroscopy (FCS) (Fradin, 2017; Krieger et al., 2015; Wang et al., 2016; Zhou et al., 2012), fluorescence recovery after photobleaching (FRAP) (Gregor et al., 2007b), single molecule tracking (Kuhn et al., 2022; Mir et al., 2018) and protein lifetime measurements (Donà et al., 2013; Durrieu et al., 2018; Khmelinskii et al., 2012). FRAP and protein lifetime measurements provide insight into the longer time dynamics of the system. Essentially, they average out sub-second processes, giving a measure of the effective dynamic parameters across the system. FCS and single molecule imaging have the advantage of measuring the local fast dynamics, but often do not provide information about longer time and spatial processes. See Huang and Saunders (2020) and Müller et al. (2013) for an extended discussion on these points. These differences have led to conflict in the measured dynamic parameters for morphogens. For example, the reported diffusion constant for eGFP::Bcd can vary from ∼1 $\mu m^2/s$ (FRAP) (Castle et al., 2011) to 7 $\mu m^2/s$ (FCS) (Abu-Arish et al., 2010). Although theoretical work has looked to integrate these measurements, taking account of the different time scales measured (Sigaut et al., 2014), there remains significant contention over the Bcd dynamics. Similar issues are pertinent in other morphogen systems, such as Nodal (Lord et al., 2021; Müller et al., 2012; Wang et al., 2016) and Wingless (Stapornwongkul et al., 2020; Stapornwongkul and Vincent, 2021). Finally, analysis of morphogen dynamics has typically focused on a fluorescently tagged version of the wild-type morphogen protein. There is a lack

[1]Warwick Medical School, University of Warwick, Coventry CV4 7AL, UK. [2]Mechanobiology Institute, National University of Singapore, Singapore 117411. [3]Department of Biological Sciences and Centre for Bioimaging Sciences, National University of Singapore, Singapore 117558. [4]Cornell University, Ithaca, NY 14850, USA. [5]Kennedy Institute of Rheumatology, University of Oxford, Oxford, OX3 7LF, UK. [6]Department of Chemistry, National University of Singapore, Singapore 117558.
*Present address: Department of Organismic and Evolutionary Biology, Museum of Comparative Zoology, Harvard University, Cambridge, MA 02138, USA.

‡Authors for correspondence (twohland@nus.edu.sg; timothy.saunders@warwick.ac.uk)

T.W., 0000-0002-0148-4321; T.E.S., 0000-0001-5755-0060



**Handling Editor: Paul François**
**Received 26 June 2023; Accepted 3 January 2024**

Development (2024) 151, dev202128. doi:10.1242/dev.202128

of quantitative data on how morphogen dynamics are altered when protein domains, e.g. DNA or receptor binding motifs, are perturbed. Despite intense study over the past 20 years, it remains a major challenge to dissect the multiple time and spatial scales that underlie morphogen dynamics, and the mechanisms that shape the gradient; such knowledge is essential for understanding of how morphogens gradients form *in vivo* (Stapornwongkul and Vincent, 2021).

Here, we take advantage of FCS combined with new Bcd mutant lines tagged with eGFP for live imaging to dissect the dynamics of Bcd with unprecedented precision. Using this, we reveal, with high accuracy, the dynamic modes that generate the Bcd gradient. We measure the Bcd dynamics at the anterior and posterior region of the embryo through nuclear cycles (n.c.) 12-14. We demonstrate that Bcd dynamics do not substantially change over n.c. 12-14, contrary to previous claims (Little et al., 2011). A two-component fit to the FCS curves is substantially better than a one-component fit in both the cytoplasm and nucleus; this implies two ('slow' and 'fast') dynamic modes in each region. The dynamics of the slower mode correspond closely to measured Bcd dynamics from FRAP. We show that the effective diffusion coefficient varies across the embryo, with it increasing towards the posterior. These results reveal that Bcd gradient formation is more complicated than previously considered. Implementing such spatial variation within a reaction-diffusion model, we show that the multiple dynamic modes can generate a long-range yet steep gradient across a large distance in a relatively short time. Finally, we explored eGFP::Bcd dynamics in a range of mutants with disrupted Bcd-binding capacity. Loss of DNA binding increases the fraction of eGFP::Bcd in the fast dynamic mode within the nucleus. In the cytoplasm, we demonstrate that the Bcd homeodomain plays a role in regulating Bcd diffusivity. Combining the Bcd homeodomain with an eGFP::NLS can reproduce the dynamics and gradient shape of the eGFP::Bcd gradient. Overall, we provide an improved version of the SDD model – involving spatially dependent dynamics – for the formation of the Bcd gradient, and we demonstrate that the Bcd dynamics are sensitive to a range of perturbations to binding elements with the protein.

## RESULTS

### Bicoid has multiple dynamic modes and these do not vary across nuclear cycles12 to 14

Previously, confocal FCS was used to measure the diffusion coefficients of eGFP::Bcd in the anterior cytoplasm (Abu-Arish et al., 2010) and anterior nuclei (Porcher et al., 2010). These measurements were limited in their position and timing within the embryo. We revisited these results, expanding the FCS measurements to both the anterior and posterior regions of the embryo during the interphases of n.c. 12, 13 and 14 (Fig. 1A,B, Fig. S1A-B). Owing to embryo curvature, our measurements were close to, but not at, the embryo poles on the dorsal surface (dashed boxes, Fig. 1A). Our FCS autocorrelation curves were highly reproducible between embryos both in the anterior domain and the posterior domain, where the brightness is very low (Fig. S1C). We co-imaged our eGFP::Bcd with H2Av::mCherry to ensure that we precisely measure in the cytoplasmic and nuclear regions during the interphase stages of nuclear cycles (n.c.) 12-14.

Comparing the normalised FCS autocorrelation curves of cytoplasm and nuclei in n.c. 12-14 (Fig. 1B, Fig. S1C), we saw no clear differences in the curves within or between cycles during interphase. These results reveal that the dynamics of eGFP::Bcd are relatively stable through n.c. 12-14, both at the anterior and posterior locations of the embryo. This contrasts with previous claims based on imaging the Bcd profile within nuclei, which predicted a decrease in Bcd diffusion in later stages: D<1 $\mu m^2\ s^{-1}$ (Little et al., 2011). We did not explore the dynamics during mitosis with point FCS because the nuclei (chromatin) move rapidly during this phase.

We next fitted dynamic models to the averaged autocorrelation curves (Fig. 1C,D). We found that a one-component model of diffusion is insufficient (Fig. S1D,E, Table S1), but a two-component diffusive model (with a fast- and slow-diffusing population) fitted the data well in all cases (Fig. 1C,D), consistent with previous FCS measurements (Abu-Arish et al., 2010; Porcher et al., 2010). We define the effective diffusion coefficient as $D_{eff}=f_{fast}D_{fast}+f_{slow}D_{slow}$, where $D_{fast}$ and $f_{fast}$ represent the diffusion coefficient and fraction for the fast dynamic mode (and similarly for the slow dynamic mode), with $f_{fast}+f_{slow}=1$. We found the effective diffusion coefficients of eGFP::Bcd in the anterior cytoplasm and nuclei were 7-9 $\mu m^2\ s^{-1}$ and 4-6 $\mu m^2\ s^{-1}$, respectively (Fig. 1E), consistent with previous observations (Abu-Arish et al., 2010; Porcher et al., 2010). Therefore, we are confident our results are reproducible and reflect accurate measurements of the eGFP::Bcd interphase dynamics.

### Bicoid dynamics are spatially dependent in both the nuclei and cytoplasm

We analysed the effective diffusion coefficient in different regions of the embryo. Strikingly, for both nuclear and cytoplasmic eGFP::Bcd, the effective diffusivity was larger in the posterior of the embryo compared with the anterior (Fig. 1E). In the posterior, the effective eGFP::Bcd diffusion coefficient in the cytoplasm and nuclei ranged from 12-15 $\mu m^2\ s^{-1}$ and 7-10 $\mu m^2\ s^{-1}$, respectively (Tables S2 and S3), a ∼1.7 fold increase compared with the anterior (Fig. S1F). We confirmed this result even if each n.c. was analysed separately (Fig. S1G).

Our FCS measurements can be used to estimate the local eGFP::Bcd concentration (Fig. 2A) (see Materials and Methods). The measured effective diffusion seems inversely correlated to eGFP::Bcd concentration (compare Fig. 1E with Fig. 2A). Our estimation of concentration uses G(0), which is inversely proportional to the number of molecules in the FCS curves. In the anterior, this estimation is reliable as there is high signal-to-noise ratio. However, in the posterior, the relative noise is higher, and so our estimate of concentration is more uncertain (Fig. S1H, see Materials and Methods). Exploring the different dynamic modes for eGFP::Bcd (Fig. 2B-D), we see that in the cytoplasm the slow dynamic mode was similar across the embryo: ∼1 $\mu m^2\ s^{-1}$ (Fig. 2C). The fast mode showed an increased diffusivity from $D_{fast}$ (*anterior*)= 13.0±2.6 $\mu m^2\ s^{-1}$ to $D_{fast}$ (*posterior*)=18.8±2.5 $\mu m^2\ s^{-1}$ (Fig. 2B, Table S2). In the nuclei, eGFP::Bcd showed a significant, although small, increase in diffusivity in the fast dynamic mode from anterior to posterior regions (9-12 $\mu m^2\ s^{-1}$ respectively), with the slow component remaining unchanged (Fig. 2B,C, Table S3).

We next asked whether the relative fractions of slow and fast components change along the embryo AP axis. In the anterior cytoplasm, the faster diffusing species comprised $f_{fast}$=65±8%, whereas in the posterior this increased to $f_{fast}$=78±6% (Fig. 2D, Table S2). We further tested the accuracy of the measured $D_{fast}$ and $D_{slow}$ values by refitting our two-particle model with the photophysical parameters (triplet states) (Fig. S2). Although the slow cytoplasmic dynamic mode was similar in both anterior and posterior of the embryo, the effective diffusion increased towards the posterior because (1) the fast dynamic mode was quicker and (2) the fraction of the eGFP::Bcd in the fast mode was larger.

Development (2024) 151, dev202128. doi:10.1242/dev.202128

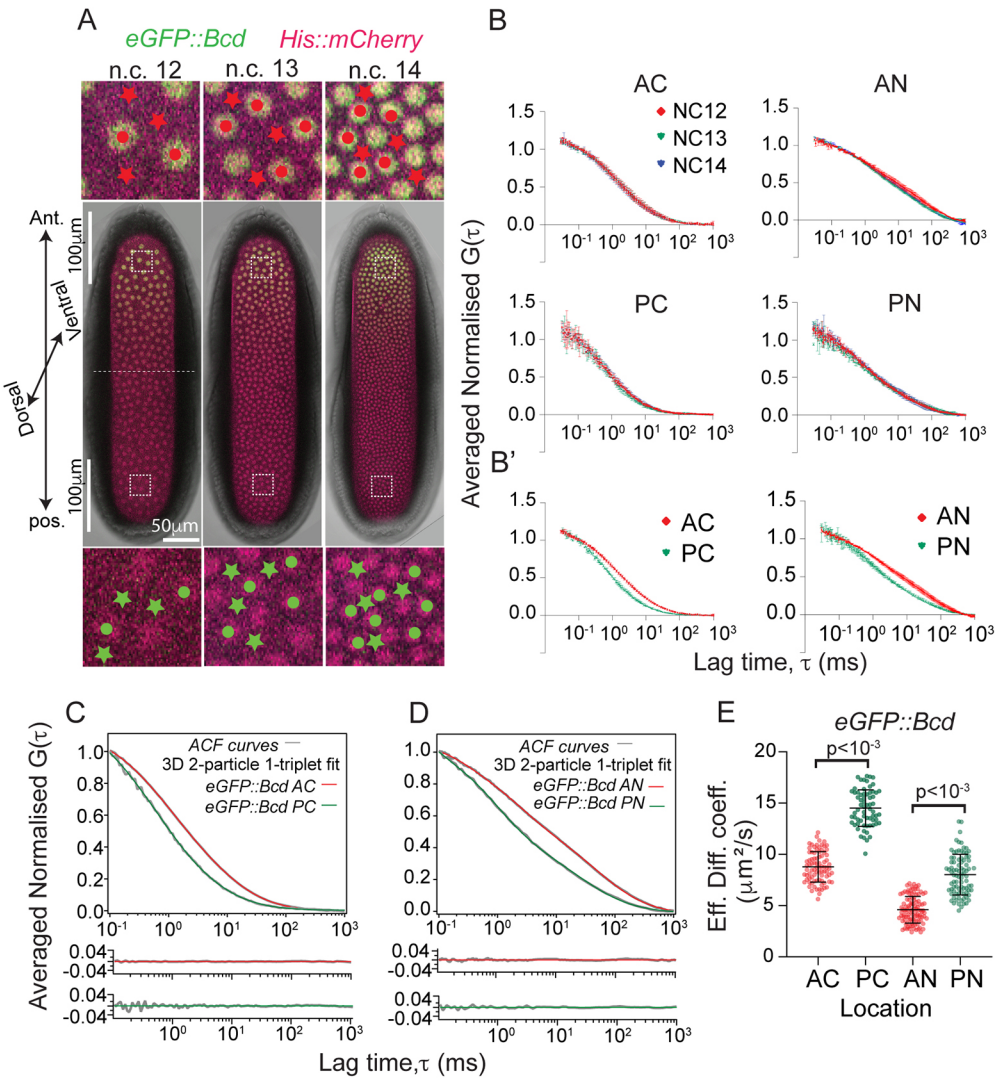


**Fig. 1. Spatio-temporal dynamics of eGFP::Bcd in the early *Drosophila* embryo.** (A) *Drosophila* blastoderm showing the interphase periods of nuclear cycles (n.c.) 12, 13 and 14. Nuclei (mCherry::His2Av, magenta) and eGFP::Bcd (green). Circles and stars indicate cytoplasmic and nuclear regions, respectively, where FCS measurements are carried out in the anterior (red) and posterior (green). The measurements are carried out within 100 µm of the anterior and posterior end of the embryo. The broken lines indicate the midline of the embryo. (B) Qualitative comparison of normalised and averaged autocorrelation (ACF) curves with mean and s.d. of eGFP::Bcd in the cytoplasmic and nuclear compartments of the n.c. 12, 13 and 14 interphases. The anterior and posterior domains are shown in the upper and lower panels, respectively. Lag times from 0.1 ms to 1 s are shown. (B′) Superimposed cytoplasmic (left) and nuclear ACF (right) curves from the anterior (red) and posterior (green). (C,D) Comparison of ACF curves (grey) with residues fitted with 3D 2-particle 1-triplet diffusion model. The comparisons are shown from 0.1 ms to 1 s lag times for visual clarity. Red and green fits correspond to anterior and posterior, respectively. (E) Scatter plot comparing the effective diffusion coefficients in different locations within the embryo: anterior cytoplasm (AC), posterior cytoplasm (PC), anterior nuclei (AN) and posterior nuclei (PN). For each condition, multiple measurements are taken from between three and five embryos in n.c. 12 to n.c. 14 (see Tables S2 and S3). Significance was calculated using a two-sided permutation test (Ho et al., 2019). $P<0.001$ indicates that diffusion values differ between anterior and posterior domains.

Likewise, in the nucleus the fraction of eGFP::Bcd in the faster dynamic mode increased towards the posterior, thereby increasing the effective diffusion coefficient (Fig. 2D, Table S3). In addition, we verified the obtained $D_{slow}$ values of confocal FCS through SPIM based FCS that captured the spatial dynamics of eGFP::Bcd simultaneously in the anterior nuclei, cytoplasm and nuclear periphery (Fig. S3).

We performed a similar analysis for eGFP::NLS, driven by the Bcd promoter region, thus forming an anterior-posterior gradient (see Materials and Methods, Fig. S4A). The results again fitted with a two-component diffusive model. The majority of the cytoplasmic eGFP::NLS was in the faster diffusive mode (Fig. 2E-H, Fig. S4, Tables S2 and S3). There was a small difference in the eGFP::NLS dynamics in the nuclei between anterior and posterior ends, possibly owing to crowding/non-specific interaction effects in the anterior where protein number is higher (Fig. 2E). Supporting this, anterior nuclei show a small but appreciable fraction (~20%) of eGFP::NLS in a slower mode (Fig. 2G,H, Table S3). eGFP::NLS diffusion is more rapid than eGFP::Bcd, with 80-95% existing in the faster diffusive mode. This is consistent with eGFP::NLS only weakly interacting with other components (e.g. itself or DNA binding and cytoplasmic elements).

In summary, the dynamics of eGFP::Bcd varies across the embryo, both in terms of the magnitude of the diffusivity and the fraction of slow- and fast-diffusing eGFP::Bcd. This means that the classic SDD model needs to be revisited as the dynamics are

Development (2024) 151, dev202128. doi:10.1242/dev.202128

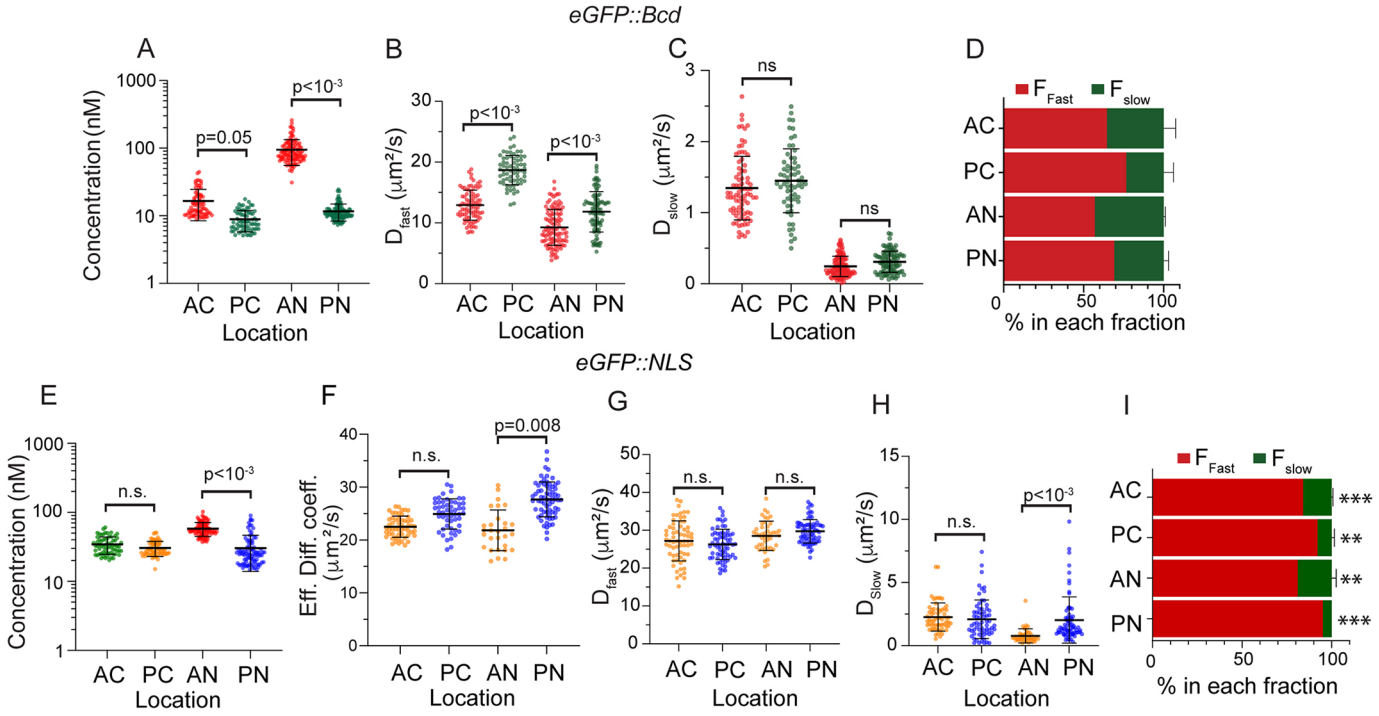


**Fig. 2. Spatial dependence in Bcd but not NLS dynamics.** (A-C) Scatter plot comparing the concentration (A), fast (B) and slow (C) diffusion components of eGFP::Bcd at different locations within the embryo. For each condition, multiple measurements are taken from between three and five embryos in n.c. 12 to n.c. 14. (D) Fraction of Bcd in fast and slow dynamic form at different locations within the embryo. (E) Effective diffusion coefficient plotted against approximated Bcd concentration. A,E are on log scale for concentration. E,G-I is same as for A-D but for eGFP::NLS. F corresponds to Fig. 1E. The significance of data in scatter plots (A-C,E-H) and bar plots (D,I) was calculated using a two-sided permutation test (Ho et al., 2019). $P$<0.001, $P$<0.01 and n.s. (not significant) indicate statistical variations in the observed concentration and diffusion values. **$P$<0.01, ***$P$<0.001 indicate statistical comparison of the fast and slow component fractions of corresponding regions between eGFP::Bcd (D) and eGFP::NLS (I).

dependent on the spatial location and/or the local morphogen concentration within the embryo.

### Formation of the Bcd gradient with multiple dynamic modes

Given distinct dynamic modes for Bcd movement exist across the embryo, we considered the effects of these on long-range gradient formation (Fig. 3A). We quantified the gradient of Bcd::eGFP and NLS::eGFP in our embryos (Fig. 3B and Materials and Methods). We see that the NLS::eGFP is noticeably shallower than the Bcd::eGFP gradient, qualitatively consistent with our measured diffusion coefficients above.

The SDD model assumes a single effective diffusion coefficient across the embryo. It can fit the data well for <300 µm along the AP-axis (see Materials and Methods), but the fit quality reduces towards the posterior (Fig. 3C), consistently underestimating the posterior concentration. To develop an improved SDD-like model of Bcd gradient formation, we need to consider: (1) Bcd has multiple dynamic modes that vary across the embryo; and (2) the observed Bcd gradient is exponential with a decay length λ=80-100 µm across most of the embryo. There are (at least) four effective modes of Bcd movement: (1) fast cytoplasmic fraction; (2) slow cytoplasmic fraction; (3) fast nuclear localised fraction; and (4) slow nuclear localised fraction. We know the fractions in each population in the anterior and posterior of the embryo (Fig. 2D). As our focus here is on the long-range establishment of the Bcd morphogen gradient, we considered the nuclear-bound fraction to be stationary, and only considered the cytoplasmic component. This assumption is supported by work showing that the Bcd gradient can form with substantially reduced Bcd nuclear import (Grimm and Wieschaus, 2010). To implement the spatially varying diffusion coefficient, we consider $D_{s,f}(x) = D^0_{s,f}\left(1+\frac{x}{x_0}\right)$ for both slow and fast cytoplasmic components. It is likely that the Bcd diffusivity is really a function of concentration (discussed below), but we use this linear form for simplicity. To account for the changes in the fraction in the slow and fast forms across the embryo, we consider the rate of cytoplasmic Bcd transition from fast to slow forms (denoted by $\beta$) to behave as $\beta(\rho_T) = \beta_0 \frac{\rho_T}{\rho_T+\rho_0}$, where $\rho_T$=$\rho_s$+$\rho_f$ is the total amount of Bcd at each position, $\rho_s$ and $\rho_f$ are the slow and fast forms of Bcd cytoplasmic concentration, respectively, and $\beta_0$, $\rho_0$ are constants. With this form, the transition rate from fast to slow forms is larger near the anterior pole.

Applying these assumptions leads to the coupled differential equations:

$$\frac{\partial \rho_s(x,t)}{\partial t} = \frac{\partial}{\partial x}\left(D_s(x)\frac{\partial}{\partial x}\rho_s(x,t)\right) - \mu_s\rho_s(x,t) - \alpha\rho_s(x,t) + \beta(\rho_T)\rho_f(x,t)$$

and

$$\frac{\partial \rho_f(x,t)}{\partial t} = \frac{\partial}{\partial x}\left(D_f(x)\frac{\partial}{\partial x}\rho_f(x,t)\right) - \mu_f\rho_f(x,t) + \alpha\rho_s(x,t) - \beta(\rho_T)\rho_f(x,t),$$

where $\mu_{s,f}$ denotes the degradation rate for the slow and fast forms, and $\alpha$ is the rate of slow-to-fast transition. For simplicity, we keep all

Development (2024) 151, dev202128. doi:10.1242/dev.202128

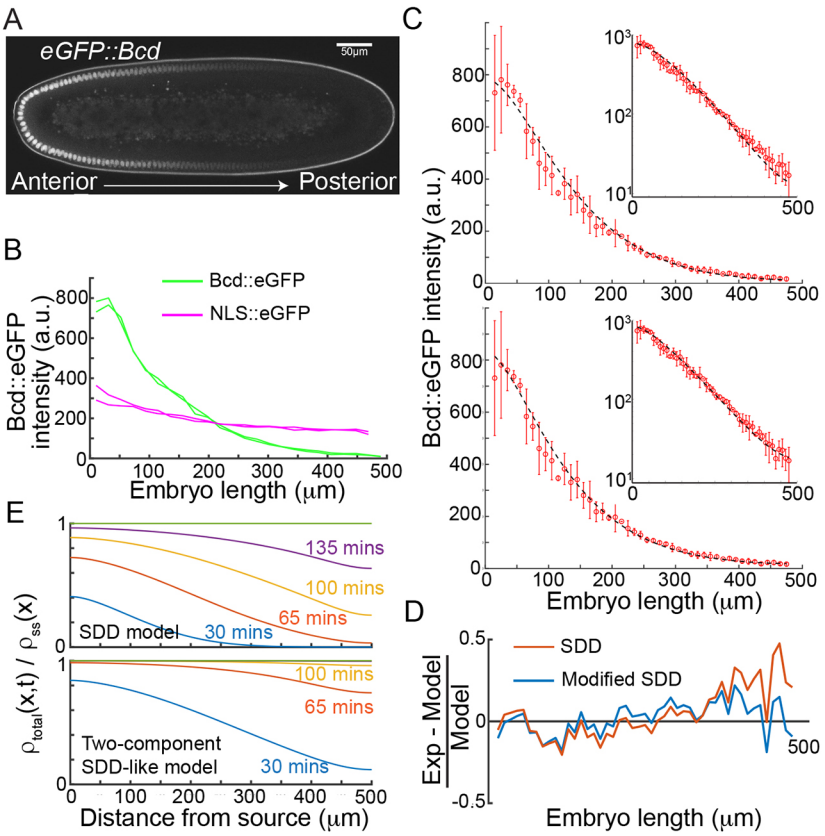


**Fig. 3. Concentration-dependent parameters within the SDD model can replicate the observed Bcd dynamics and gradient.** (A) Embryo expressing eGFP::Bcd, showing the gradient from anterior (left) to posterior (right). (B) Two example profiles for Bcd::eGFP (green) and NLS::eGFP (magenta) normalised from Histone mCherry background fluorescence. (C) Top: SDD model prediction for the formation of the Bcd gradient (dashed black line) compared with experimental profiles (red circles, mean±s.d., $n$=3). Inset shows the same on a log intensity scale. Bottom: the same as above but with a fit from the modified 2-component SDD model (see supplementary Materials and Methods). (D) Relative fitting precision of the two models from (C) along the embryo AP axis. (E) Evolution of gradient formation for the SDD model (top) and modified 2-component SDD model (bottom). *Y*-axis is the relative difference from steady-state at each position (value of 1 indicates being in a steady-state).

parameters constant that are not explicitly highlighted as having a functional dependence. Implementing parameters based on our above and other *in vivo* measurements (Abu-Arish et al., 2010; Drocco et al., 2011; Durrieu et al., 2018), we can fit the n.c. 14 Bcd gradient as a function of position (Fig. 3C,D). In the supplementary Materials and Methods, we discuss other potential model variations and the resulting fit quality (Fig. S5, Table S7). The additional of fast and slow populations allows a more accurate fit to the Bcd profile (Fig. 3D), although this is arguably unsurprising given the increased parameter space.

Are there other advantages by having multiple dynamic modes? Given the large value for $D_{fast}$, we postulated that the rate of gradient formation in the posterior will be more rapid in the two-component model. Comparing the SDD model with our modified two-component version (Fig. 3E), we see that the morphogen reaches the posterior more rapidly with two dynamic components. We note that in the posterior the absolute concentration differences between the models is not large, but there is a substantial change in the relative concentration differences from steady-state as a function of time.

We can estimate the time taken for a molecule to move from the anterior to posterior poles. The time taken for a molecule to diffuse an average distance $x_{rms}$ is given by $t\tilde{x}^2_{rms}/(cD)$, where the constant $c$ depends on the system dimensionality. Taking $D{\approx}7\ \mu m^2\ s^{-1}$, $x_{rms}{\approx}450\ \mu m$ and $c$=4 (representing effectively 2D diffusion near the surface) gives $t{\approx}2$ h. This is two to four times the Bicoid lifetime – i.e. fewer than 10% of the molecules that may diffuse a sufficient distance are also likely not to degrade within that time. In the case of $D{\approx}18\ \mu m^2\ s^{-1}$, this time is more than halved.

From this analysis, we see three important points: (1) having slow and fast forms of Bcd leads to more rapid gradient formation at larger distances (Fig. 3E); (2) the increased fraction in the fast form results in increased concentration in the posterior compared with a simple SDD model (Fig. 3D), consistent with experimental observation of Bcd in the most posterior (Mir et al., 2017); (3) even with the multiple species and varying diffusion, the gradient is still exponential across a large extent, consistent with experimental observations (Fig. 3B, see Materials and Methods for details of gradient quantification and error estimation) (Gregor et al., 2007b).

How do these different dynamic modes arise? They are not a simple consequence of spatial differences across the embryo, as the eGFP::NLS results show no such spatial dependence. In the next sections, we explore perturbations to binding elements of Bcd to dissect possible mechanisms driving the observed behaviour.

## Bicoid DNA binding determines the slow diffusion dynamics within the nucleus

Given our above observations, we investigated the possible mechanisms regulating Bcd diffusivity. Bcd is a transcription factor known to cooperatively bind to DNA (Burz et al., 1998; Lebrecht et al., 2005). Furthermore, Bcd binds to *caudal* mRNA in the BRE (Bicoid response element) of the *caudal* 3′UTR, repressing its translation in the cytoplasm (Niessing et al., 2002, 1999, 2000). Therefore, we hypothesised that direct DNA/RNA binding impacts Bcd dynamics.

The Bcd homeodomain mutation $bcd^{N51A}$ leads to loss of downstream target expression (e.g. *hunchback*), posited due to disruption of Bcd DNA-binding efficacy (Niessing et al., 2000). It also has a reported role in reducing the repression of *caudal* expression by Bcd in the cytoplasm. Another homeodomain mutation, $bcd^{R54A}$, is also reported to de-repress caudal expression but it has normal *hunchback* expression (Niessing et al., 2000). To test whether these mutations in Bcd alter the protein dynamics, we generated eGFP::Bcd$^{N51A}$ and eGFP::Bcd$^{R54A}$ (Fig. 4A). These

Development (2024) 151, dev202128. doi:10.1242/dev.202128

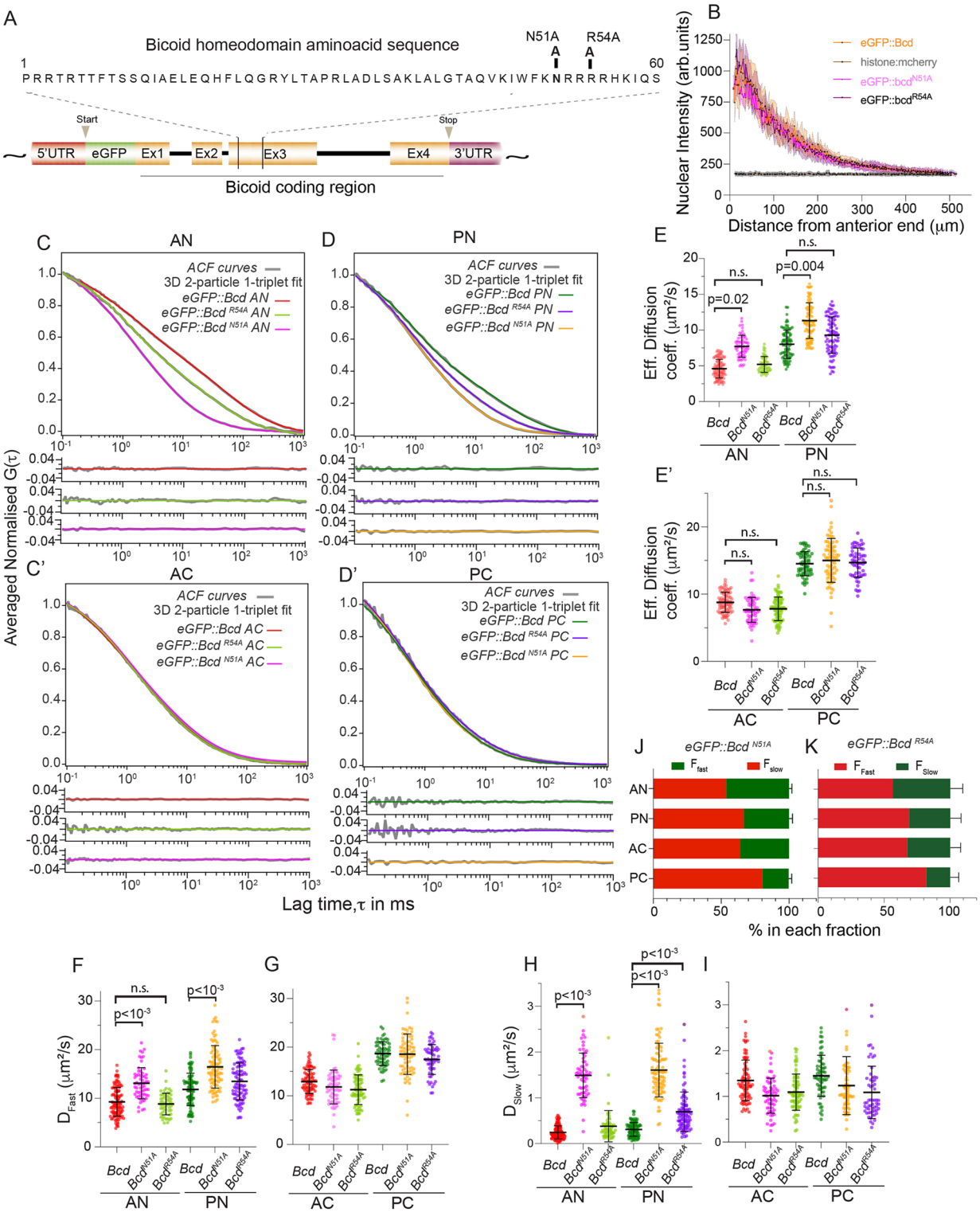


**Fig. 4. Bcd homeodomain alters nuclear Bcd dynamics.** (A) Schematic of *Drosophila bcd* genomic region. A 60 amino acid region constituting the *bcd* homeodomain is expanded. Amino acid conversion at position 51 from asparagine to alanine (N51A) and at position 54 from arginine to alanine (R54A) is displayed. (B) Gradient profile to embryo length plot of the midsagittal sections of eGFP::bcd$^{N51A}$, eGFP::bcd$^{R54A}$, eGFP::bcd and mCherry::His2Av. (C-D′) Comparison of averaged normalised ACF curves (grey) of eGFP::Bcd, eGFP::Bcd$^{N51A}$ and eGFP::Bcd$^{R54A}$ with residues fitted with 3D 2-particle 1-triplet diffusion model. Red and green fits correspond to nuclear and cytoplasmic regions in anterior and posterior regions, respectively for eGFP:Bcd. Magenta and orange fits correspond to eGFP::Bcd$^{N51A}$. Light green and purple fits correspond to eGFP::Bcd$^{R54A}$. (E,E′) Comparison of the effective diffusion coefficients of eGFP::Bcd, eGFP:Bcd$^{R54A}$ and eGFP::Bcd$^{N51A}$ in the nucleus (E) and cytoplasm (E′). (F-I) Scatter plots comparing $D_{fast}$ (F,G) and $D_{slow}$ (H,I) of eGFP::Bcd$^{N51A}$ and eGFP::Bcd$^{R54A}$ at different locations within the embryo. Anterior cytoplasm (AC), posterior cytoplasm (PC), anterior nuclei (AN) and posterior nuclei (PN). (J,K) Bar plots indicating fractions (%) of fast- and slow-diffusing eGFP::Bcd$^{N51A}$ (J) and eGFP::Bcd$^{R54A}$ (K) molecules in the corresponding embryo compartments. The significance of scatter plots was tested using a two-sided permutation test (Ho et al., 2019). $P$<0.0001, $P$<0.001, $P$<0.05 and n.s. (not significant) indicate statistical comparison of observed diffusion values. All error bars indicate±1 s.d.

Development (2024) 151, dev202128. doi:10.1242/dev.202128

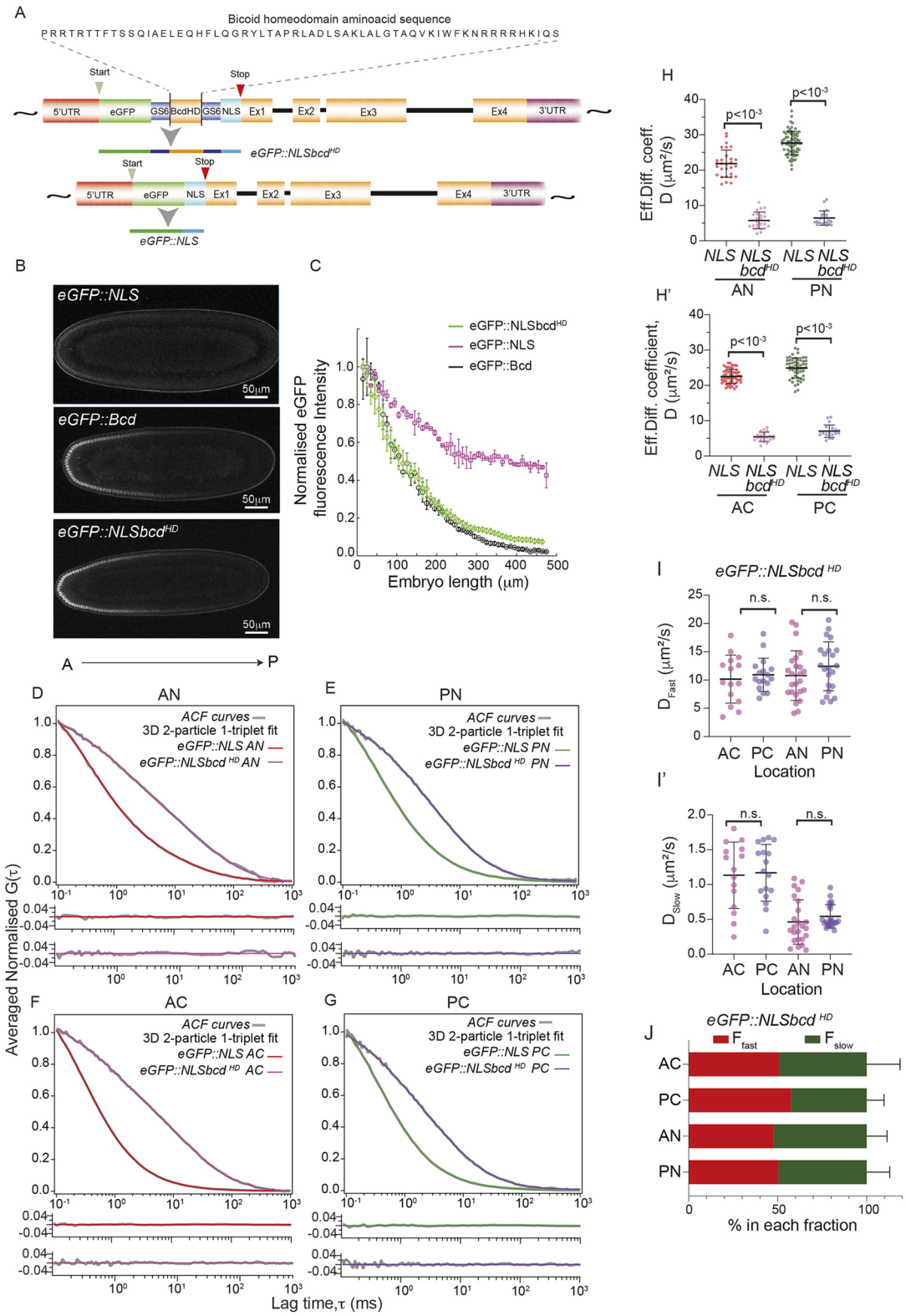


**Fig. 5. Effects on dynamics of adding the *Bcd* homeodomain to NLS.** (A) Schematic of the construction of the eGFP::NLS and eGFP::NLSbcd$^{HD}$ lines. The *bcd* homeodomain is inserted between eGFP and NLS flanked by GS6 linker to generate eGFP::NLSbcd$^{HD}$. (B) Midsagittal sections of *Drosophila* embryos at n.c.14 expressing eGFP::NLS (top), eGFP::Bcd (middle) and eGFP::NLSbcd$^{HD}$ (bottom). (C) Comparison of normalised gradient profiles between eGFP::NLS (magenta), eGFP::NLSbcd$^{HD}$ (green) and eGFP::Bcd (black). Dashed lines indicate the standard deviation of gradient profiles. (D-G) Comparison of averaged normalised ACF curves (grey) of eGFP::NLS and eGFP::NLSbcd$^{HD}$ with residues fitted with 3D 2-particle 1-triplet diffusion model. Red and green fits correspond to nuclear and cytoplasmic regions of anterior and posterior of eGFP::NLS, respectively. Magenta and violet fits correspond to eGFP::NLSbcd$^{HD}$. (H,H′) Comparison of the effective diffusion coefficients of eGFP::NLS and eGFP::NLSbcd$^{HD}$ for nuclei (H) and cytoplasm (H′). (I,I′) Scatter plots comparing $D_{fast}$ (I) and $D_{slow}$ (I′) for eGFP::NLSbcd$^{HD}$. (J) Bar plots indicating fractions (%) of fast- and slow-diffusing eGFP::NLSbcd$^{HD}$ molecules in the corresponding embryo compartments. *P*-values calculated using a two-sided permutation test (Ho et al., 2019). All error bars indicate±1 s.d.

Development (2024) 151, dev202128. doi:10.1242/dev.202128

embryos show a clear anterior-to-posterior gradient of Bcd (Fig. 4B).

We performed FCS on eGFP::Bcd$^{N51A}$ embryos at different locations within n.c. 12-14 embryos (Fig. S6, Table S4). In the nucleus, the normalised autocorrelation curves for eGFP::Bcd$^{N51A}$ embryos were clearly different from eGFP::Bcd embryos, with faster dynamics (Fig. 4C-E). However, the dynamics in the cytoplasm were not significantly altered (Fig. 4C′-E′). The effective diffusion coefficients further reveal that the diffusion of eGFP::Bcd$^{N51A}$ in the anterior nuclei was 7-9 µm$^2$ s$^{-1}$ and in the posterior it was 9-13 µm$^2$ s$^{-1}$ (Fig. 4E, Table S4).

In the nucleus, both the fast and slow modes in eGFP::Bcd$^{N51A}$ embryos show increased diffusivity compared with eGFP::Bcd embryos (Fig. 4F-I). Although the increase in the slow mode was expected due to the loss of Bcd binding to the DNA, the reason for the change in the fast mode is less clear. These effects are apparent in both the anterior and posterior of the embryo (Fig. S6). As with eGFP::Bcd, the slow mode diffusivity in eGFP::Bcd$^{N51A}$ embryos was similar across the embryo (Fig. 4H), with the diffusion coefficient of the fast component increasing towards the posterior (Fig. 4F). The relative fractions of eGFP::Bcd$^{N51A}$ in the slow and fast modes also changed from anterior to posterior (Fig. 4J), with a larger fraction of eGFP::Bcd$^{N51A}$ being in the faster diffusive mode within the posterior nuclei. These results demonstrate that homeodomain function influences the Bcd diffusion dynamics, at least in the nuclei.

The dynamics of eGFP:Bcd$^{R54A}$ embryos were more similar to eGFP::Bcd (Fig. 4F-K, Fig. S7). There is little difference in the measurements for the diffusion coefficients in nuclei. This is consistent with the R54A mutation not affecting hunchback expression (Niessing et al., 2000). There is a decrease in $D_{slow}$ in the posterior, suggesting that the disrupted interaction with *caudal* may be altering posterior Bcd dynamics.

In addition to the homeodomain, the YIRPYL motif and the PEST domain are involved in Bcd-mediated *caudal* mRNA repression. Point mutations in these *bcd* domains are known to abolish the caudal repression in the cytoplasm (Niessing et al., 2002, 1999). Conversions of tyrosine (Y) to alanine (A) and leucine (L) to arginine (R) in the YIRPYL motif (YIRPYL→AIRPYR) abolishes *caudal* repression in the cytoplasm by breaking the interaction of Bcd with the translation initiation factor, eIF4E, at the 5′cap *caudal* RNA (Niessing et al., 2002). Furthermore, replacing four threonine (T) and one serine (S) residues to five alanine (A) residues (Bcd$^{5aa}$) in the PEST domain at positions 188, 193, 195, 197 and 200 abolishes *caudal* repression (Niessing et al., 1999). The above mutations may still have residual interacting elements of Bcd to *caudal* mRNA. To test the effect of removing all these binding elements on Bcd dynamics, we generated eGFP:Bcd multi-mutant (MM) line that harbours mutations in the PEST (Bcd$^{5aa}$) domain along with homeodomain N51A and YIRPYL motif (AIRPYR) (Fig. S8A). We refer this line as eGFP::Bcd$^{MM}$. FCS measurements of eGFP::Bcd$^{MM}$ embryos in the anterior cytoplasm and nuclei revealed similar Bcd dynamics to eGFP::bcd$^{N51A}$ embryos both in slower and faster Bcd dynamics (Fig. S8, Table S5).

Our results for the N51A, R54A and *bcd$^{MM}$* alleles suggest that: (1) the Bcd homeodomain plays an important role in determining Bcd dynamics; (2) Bcd binding to *caudal* mRNA alone is insufficient to explain the Bcd cytoplasmic dynamics; and (3) there are likely other components (either within Bcd itself or other proteins) in the cytoplasm that affect Bcd dynamics at different Bcd concentrations.

### The Bcd homeodomain regulates protein dynamics in both the nucleus and cytoplasm

Given our above results, combined with the presence of putative cytoplasmic interaction sites within the Bcd homeodomain (Burz et al., 1998; Lebrecht et al., 2005; Ling et al., 2019; Ma et al., 1996; Niessing et al., 1999; Yuan et al., 1996), we hypothesised that the Bcd homeodomain alone (without the rest of the Bcd protein) may be sufficient to replicate, at least partially, the observed Bcd protein dynamics.

To test this hypothesis, we fused the *bcd* homeodomain to eGFP::NLS, which we refer to as eGFP::NLSbcd$^{HD}$ (Fig. 5A). We compared the gradient profiles of eGFP:NLS, eGFP:: NLSbcd$^{HD}$ and eGFP::Bcd (Fig. 5B,C). Consistent with our prediction, the gradient of eGFP::NLSbcd$^{HD}$ was steeper than eGFP::NLS (Fig. 5C). Remarkably, the eGFP::NLSbcd$^{HD}$ concentration gradient closely matched the eGFP::Bcd profile (Fig. 5C), with only an increased concentration towards the posterior. This is consistent with the lifetime of eGFP::NLSbcd$^{HD}$ being longer than eGFP::Bcd. This strongly suggests that the homeodomain interactions in the cytoplasm and nuclei are significant contributors to determining Bcd dynamics.

Next, we performed FCS of eGFP::NLSbcd$^{HD}$ embryos to explore the dynamic modes (Fig. 5D-G, Fig. S9, Table S6). Interestingly, there were no anterior-posterior differences in the diffusion coefficients of eGFP::NLSbcd$^{HD}$ embryos (Fig. 5H,H′, Fig. S9A″). This supports the conclusion that the anterior-posterior dynamic changes are due to interactions of the Bcd protein with itself or other elements, and not, for example, due to differences in the physical environment between the anterior and posterior. For eGFP:: NLSbcd$^{HD}$, the slow and fast populations represented ∼50% each at all positions within the embryos (Fig. 5J). There is ∼3.5- to 4.5-fold decrease in the effective diffusion coefficients of eGFP::NLS (Fig. 5H,H′) upon addition of the homeodomain to NLS encompassing ∼2.5-fold decrease in both $D_{fast}$ and $D_{slow}$ values (Fig. S9B-E). Furthermore, the fraction of eGFP::NLSbcd$^{HD}$ in the slower form ($F_{slow}$) significantly increased compared with eGFP:: NLS (compare Fig. 2I and Fig. 5J). We note that $D_{slow}$ in the nuclei and cytoplasm (0.5 µm$^2$ s$^{-1}$ and 1 µm$^2$ s$^{-1}$) are comparable between eGFP::NLSbcd$^{HD}$ and eGFP:Bcd (0.2-0.3 µm$^2$ s$^{-1}$ and 1 µm$^2$ s$^{-1}$) embryos. This suggests that homeodomain binding affinities to nuclear DNA and cytoplasmic RNA or cytoplasmic elements are different, and this may regulate the slow Bcd diffusive mode. However, $D_{fast}$ displays distinct differences between eGFP:: NLSbcd$^{HD}$ and eGFP:Bcd; the homeodomain is not sufficient to replicate all the Bcd protein dynamics.

## DISCUSSION

We have provided a detailed analysis of Bcd morphogen dynamics in both space and time. Our FCS measurements demonstrate that eGFP::Bcd has both highly motile and slower fractions, in both the nucleus and the cytoplasm. Crucially, these dynamics are spatially varying across the embryo. Given the changing fractions of the fast and slow populations in space, the interactions between the populations are likely non-linear, and dependent on the local eGFP::Bcd concentration. The resulting dynamics generate a gradient across the whole embryo. Although there is no known role for Bcd in the embryo posterior, it has recently been shown that Bcd influences boundary specification at 70% EL (around 350 µm from the anterior) (Singh et al., 2022).

FRAP measurements of eGFP::Bcd in the cytoplasm have reported an effective diffusion coefficient in the range of 1 µm$^2$ s$^{-1}$ (Abu-Arish et al., 2010; Castle et al., 2011). Our measurements of

Development (2024) 151, dev202128. doi:10.1242/dev.202128

the cytoplasmic slow fraction ($D_{slow}$~1 μm$^2$ s$^{-1}$) are consistent with this. Second, distinct clusters of eGFP::Bcd have been observed in the embryo posterior (Mir et al., 2017). Even with an effective diffusion coefficient of 7 μm$^2$ s$^{-1}$, few molecules would be expected at the posterior given the estimated Bcd lifetime (30-50 min) (Fig. 3E). We show that eGFP::Bcd in its fastest form can move quickly (~18 μm$^2$ s$^{-1}$), and the fraction of eGFP::Bcd in this form increases at lower concentrations. We note, however, that the relationship between Bcd diffusivity and concentration are correlative (also see Fig. S13E,F); we have not directly tested that altered Bcd concentration affects the Bcd diffusion coefficient. Given the fast population of Bcd, it is possible for a subpopulation of eGFP::Bcd to reach the posterior within the first 90 min of development, while the majority of eGFP::Bcd forms a steep concentration profile (Fig. 3D). This is consistent with theoretical predictions, which also postulated that Bcd may have spatially varying dynamics (Sigaut et al., 2014). The SDD model provides a good estimate of the Bcd gradient profile and the 'average' dynamics. However, it is inconsistent with Bcd puncta in the posterior pole, the speed of gradient formation in the posterior and our measurements of spatially varying diffusivity. Here, we present a modified SDD model, where the diffusion component is itself spatially varying. However, we emphasise that this model is phenomenological; it will be interesting to dissect further the specific mechanisms driving the non-linear dynamics we observe.

These results suggest that: (1) Bcd DNA binding plays an important role in determining Bcd dynamics within the nucleus and (2) the dynamics of Bcd within the nucleus are more complicated than a simple model of bound versus unbound Bcd (Fradin, 2017). This might point towards anomalous diffusion as the dominant diffusive mode (Höfling and Franosch, 2013), in which, instead of two distinct diffusion components, the diffusion coefficient is scale dependent. In fact, the anomaly parameter can provide a good empirical measure for changes in molecular interactions (Fradin, 2017). However, the anomalous and two-component fit cannot be easily differentiated, and the two-component model provides a simpler model and clearer interpretation of the changes due to binding. There may be other modes that are not considered, but our approach – given the excellent fit to the FCS profiles – appears to approximate well the underlying dynamics. We include binding/unbinding within our model. Our evidence suggests that the dynamics in the nucleus are driven by DNA binding/unbinding. Yet the dynamics are less clear in the cytoplasm and it is an assumption of our phenomenological 2-state model that Bcd can reversibly move between fast and slow cytoplasmic forms.

Bcd maintains a similar profile across multiple nuclear cycles (Gregor et al., 2007b). The presence of a rapidly diffusing pool can (at least partially) help to re-establish the gradient quickly after each division. It has also been proposed that Bcd can be produced throughout the embryo, without need for long-ranged diffusive movement (Spirov et al., 2009). Yet our results suggest that >50% of eGFP::Bcd exists in a rapidly diffusing form ($D$>5 μm$^2$ s$^{-1}$) that will 'wash out' a locally produced gradient. To summarise, our results provide a mechanism for Bcd to have both slow dynamics (as measured by FRAP) and rapid movement (measured in FCS), which set up the gradient across the embryo in a few hours, largely driven by hindered diffusion. A caveat to this conclusion is that previous analysis of Bcd::eGFP profiles suggested that Bcd dynamics become constrained in n.c. 13 and 14 (Little et al., 2011). Our results show that there still exists a dynamic pool of Bcd at these times. However, local barriers between nuclei – particularly during cellularisation – may impede long-range Bcd movement. To test this idea, we used SPIM-FCS to explore the local spatial distribution of diffusion of Bcd::eGFP around the nucleus (Fig. S3). We see a clear reduction in Bcd::eGFP diffusivity around the nuclear envelope, consistent with slow movement in/out of the nucleus during interphase. However, we note that this approach does not capture the fast diffusive mode (owing to limitations in camera speed).

We have also tried to dissect the specific interaction elements of Bcd that drive its dynamics. In the nucleus, the two populations can be largely (though not completely) explained by Bcd binding to DNA. We have shown in the cytoplasm that the ability to transform the eGFP::NLS gradient into one that qualitatively matches the eGFP::Bcd gradient through the addition of the Bcd homeodomain suggests that this region of Bcd is crucial in determining Bcd dynamics. Our eGFP::NLSbcd$^{HD}$ construct does not show concentration/spatial dependence, suggesting that the homeodomain is not wholly sufficient to explain the Bcd dynamics. It is possible that Bcd interacts with cytoplasmic elements, including actin and microtubule structures (Cai et al., 2017), which alter its diffusivity. We also observe evidence for non-specific binding in the *bcd$^{N51A}$* embryos and also in the NLS::eGFP nuclear anterior fraction. This is consistent with non-specific DNA interactions (Vukojević et al., 2010), but further work is required to dissect these interactions.

Such spatially varying dynamics have been hypothesised previously (Lipkow and Odde, 2008). The subcellular gradient of MEX-5 within the *C. elegans* embryo has spatially varying dynamics, due to interactions mediated by polarised distribution of PAR proteins (Griffin et al., 2011), and a recent study in *Xenopus* extracts has shown that cytoplasmic organisation can alter protein diffusivity (Huang et al., 2022). In single molecule tracking of Nodal, multiple dynamic modes have been observed (Kuhn et al., 2022). In our case, there are no known significant structural differences in the anterior and posterior ends of the embryo at this stage, nor are there gradients of polarity. Our results suggest that the Bcd homeodomain has a role in regulating the protein dynamics in the cytoplasm. Bcd binds to the BRE (Bicoid response element) in the *caudal* 3′UTR and it also binds to the 5′cap of the *caudal* mRNA through its PEST domain via adaptor proteins (Cho et al., 2005; Macdonald, 2005; Niessing et al., 2002, 1999, 2000). Our results with the N51A and bcd$^{MM}$ lines reveal Bcd binding to *caudal* is unlikely to have a major impact on the diffusion of Bcd in the cytoplasm. One future test of this result is to measure Bcd dynamics in embryos over- or underexpressing *caudal*. On the other hand, our results with NLSbcd$^{HD}$ show that the *bcd* homeodomain does impact protein dynamics in the cytoplasm. However, the specific domains behind this behaviour remain unclear. There are additional factors, such as Zelda, that may also play a role in spatially varying the effective Bcd dynamics (Drocco et al., 2011). Finally, we observe that the relative fraction of Bcd in the fast/slow forms spatially varies across the embryo. This suggests that the transition between the slow and fast cytoplasmic forms is non-linear, and in particular may depend non-linearly on the local Bcd concentration. More refined spatial dissection of the dynamics will help to illuminate this behaviour more clearly. Such behaviour may enable Bcd to adapt to embryos of variable size (Huang et al., 2020). One possible other factor may be cytoplasmic flows, which have recently been demonstrated to play a role in refining the Bcd gradient (Hernandez-Lopez et al., 2023).

Bcd operates as a morphogen within the *Drosophila* blastoderm. Are our observations potentially relevant for other morphogens, which are typically extracellular ligands? Molecules can be hindered either passively due to micro-geometries of the diffusing

Development (2024) 151, dev202128. doi:10.1242/dev.202128

environment (Kuhn et al., 2022) or actively stalled by binding and unbinding of the specific receptors on the cell surfaces or transient binding of interacting proteins (Müller et al., 2013). Recent evidence in Nodal suggests that its movement is akin to hindered diffusion (Kuhn et al., 2022), resulting in an exponential morphogen distribution. During expansion of *Drosophila* wing imaginal discs, the distribution of Dpp activity can be scaled to the size of the tissue via pentagone (Hamaratoglu et al., 2011), a feedback regulator of Dpp, and by Dpp recycling (Romanova-Michaelides et al., 2022). In both the above examples, feedback between the cellular environment (including receptor distribution) and the morphogen dynamics sets up the gradient. Our results indicate that Bcd dynamics can be also considered as hindered diffusion in the *Drosophila* blastoderm; a balance between diffusion and interactions with the local region (at least in part mediated by the Bcd homeodomain) generates the effective dynamics that create the Bcd gradient. It seems likely that, in the cytoplasm, Bcd movement is hindered by the cytoskeletal structures, which could be pertinent for extracellular morphogens. Therefore, we predict that our key observation – that the effective morphogen dynamics are not constant in space – will be relevant for other morphogen systems.

We have used dual colour imaging to ensure that we are recording accurately either nucleus or cytoplasmic pools. An alternative strategy is to use imaging-FCS (Fig. S3) (Krieger et al., 2015). With this approach, the available timescales are reduced (lowest time resolution about 0.1 ms) but spatial cross-correlation can be explored. This approach has the advantage of being able to image throughout mitosis, as spatial movements of nuclei can be accounted for. It will be interesting to explore how Bcd dynamics change during nuclear division in the blastoderm.

Overall, the combination of new Bcd mutant eGFP lines with careful FCS measurements has revealed insights into how a morphogen gradient can form across the required spatial and temporal scales. The apparent concentration-dependent dynamics of Bcd provides a mechanism for how the Bcd gradient can form sufficiently quickly while also having slower more local dynamics. Outstanding questions include: (1) what interactions are determining Bcd dynamics in the cytoplasm; (2) is Bcd diffusivity concentration dependent and, if so, how; and (3) do other morphogens display position and/or concentration-dependent dynamics?

## MATERIALS AND METHODS

### Generation of fly lines

eGFP::Bcd fly line was a gift from Thomas Gregor (Princeton University, NJ, USA). The eGFP::Bcd line was generated by introducing eGFP coding region into the N-terminus of the *bcd*-coding region after the start codon in the pCaSpeR7 Bcd plasmid (Barolo et al., 2000; Hazelrigg et al., 1998; Thummel and Pirrotta, 1992). eGFP tagged Bcd was brought in the background of $bcd^{E1}$ null allele to ensure that it is the only source of Bcd in these embryos. eGFP::Bcd was crossed with His2A::mCherry (Krzic et al., 2012) to mark the nuclei of early blastoderm embryos, such that the 560-laser line could act as a reference to mark the nucleus and to differentiate the cytoplasmic region in the syncytium. eGFP::$Bcd^{N51A}$, eGFP::$Bcd^{R54A}$ and eGFP::$Bcd^{MM}$ mutant lines were generated by PCR. For N51A and R54A, the Asn (N) at position 51 and Arg (R) at position 54 of Bicoid homeodomain, respectively, are edited to Ala, as generated by Niessing et al. (2000). The PstI-SalI fragment of the Bicoid homeodomain sequence bearing appropriate base pair changes (N51A and R54A) replaces the existing PstI-SalI fragment of the eGFP::Bcd pCaSpeR7 plasmid by restriction digestion. Likewise, multi-mutant eGFP::Bicoid (eGFP::$bcd^{MM}$) is generated through sequential editing in eGFP::$Bcd^{N51A}$ pCaSpeR7 construct background. Fragments containing the mutant YIRPYL motif (AIRPYR) (Niessing et al., 2002) and the mutant PEST ($bcd^{5aa}$) domain of Niessing et al. (1999) are reintroduced and replace the existing fragments of the eGFP::$Bcd^{N51A}$ pCaSpeR7 construct. Therefore, eGFP::$Bcd^{MM}$ bears targeted mutations in the homeodomain (N51A), YIRPYL motif and PEST domain (Figs 4A and Fig. S8A).

For control, we generated an eGFP::NLS line expressed using the Bcd regulatory sequences as described by Gregor et al. (2008). We introduced a PCR amplified fragment containing a single copy of the SV40 nuclear localisation sequence and a stop codon (NLS-STOP) in between the eGFP sequence and Bcd-coding region in the eGFP::Bcd pCasper7 plasmid explained in the preceding paragraph (illustrated in Fig. 5A). Upon translation, only the eGFP::NLS part of the eGFP-NLS-Bcd mRNA is expressed, generating a gradient across the A-P axis of the embryo (Fig. S4A; Fig. 5B) (Gregor et al., 2008). We generated the eGFP::NLS$bcd^{HD}$ line by introducing the homeodomain sequence of Bcd that encodes 60 amino acids. We PCR amplified the 180 bp homeodomain sequence from exon 3 of the Bcd genomic region using primers that had a $GS_6$ linker and Kpn1 restriction site at their extreme ends. The Kpn1-$GS_6$-$bcd^{HD}$-$GS_6$-Kpn1 fragment was digested and inserted into the newly introduced Kpn1 site (between eGFP and NLS-STOP) of the acceptor eGFP::NLS pCaSpeR7plasmid. In all cases, the eGFP sequence used is from eGFP::Bcd pCaSpeR7, which belongs to eGFP(F64L/S65T) (Gregor et al., 2007b; Patterson et al., 1997). All transgenic lines were injected and generated by Bestgene.

### Preparation of embryos for FCS measurements

eGFP::Bcd; His2A::mCherry embryos at n.c. 9 were dechorionated and mounted in PBS on a coverslip in such a way that the dorsal surface of the embryo struck to the surface of the coverslip and faced the objective. The dorsal surface is flatter compared with the curved ventral surface and the dorsal surface covers a larger area with shorter *z*-depth. The cortical planar surface of the embryo, which contained the maximum number of in-focus nuclei, was selected for FCS measurements (Fig. 1A). His2A::mCherry marked nuclei and was used as a reference for the nuclear Bcd FCS measurements; the area devoid of His2A::mCherry was used for the cytoplasmic Bcd measurements. Typically, the FCS measurements were performed for 60 s in the cytoplasm and for 20-40 s in the nuclei. The reduction in the duration of nuclear measurements were due to fluctuation of the nuclear positions during imaging.

### FCS measurements

FCS was carried out using a FV1200 confocal microscope (Olympus) equipped with a time-resolved FCS upgrade kit (PicoQuant) at 25°C. The 488 nm pulse wave laser line was used to excite eGFP::Bcd through an UplanSApo 60× NA 1.2 water immersion objective (Olympus). The laser power was optimised using nuclear eGFP::Bcd at n.c. 14. Laser powers of 2-3 µW, which had better signal-to-noise ratio and minimal photobleaching, were used for FCS measurements both in the nucleus and cytoplasm regions of the anterior and posterior domains of the embryo (Fig. S10). The fluorescence emission was passed through a 405/488/543/635 dichroic mirror (Chroma Technology), a confocal pinhole of one airy unit (120 µm) and then split using a 50/50 mirror plate. The split emission was detected simultaneously by an avalanche photodiode (SPCM-AQR14; PerkinElmer). Dual detector measurements effectively remove after-pulsing information in the FCS curves. The photon counts from the detector were registered by a TimeHarp 260 time-correlated single-photon counting board (PicoQuant) and processed by the SymPhoTime (Kapusta, 2010) software (PicoQuant). The same software was also used to calculate the auto-correlation function. For further details on FCS calibration, see supplementary Materials and Methods.

### Qualitative comparison of ACF curves

ACF curves of individual measurements were normalised and compared to show their qualitative differences. The ACF curves were normalised as $G(\tau)-G(\infty)/G(0)-G(\infty)$. $G$ (0) is the amplitude of the ACF curves (typically at lag time 0.0001 s), $G$ ($\infty$) is the convergence value at the longer lag times (typically 1 s). The curves and graphs are plotted in GraphPad Prism version 10.0.0.

### FCS curve fitting

The FCS curves of each measurement were fitted by three-dimensional diffusion models involving diffusion of 1 and 2 species with and without reversible

switching of the fluorophores to dark states, using Igor-Pro (8.03), FCS data processing plug-in, Version 2.1, https://www.dbs.nus.edu.sg/lab/BFL/confocal_FCS.html. See supplementary Materials and Methods for further details.

### Estimation of eGFP::Bcd concentration in the measurement volume

We estimated the concentration of eGFP::Bcd and eGFP::NLS through generating a standard curve (Fig. S11). A high known concentration of Atto-488 dye was serially diluted to lower concentrations (10, 7, 5 and 2 nM) and the correlation amplitudes determined. Similarly, known concentrations (3, 4, 6 and 15 nM) of eGFP *in vitro* solutions were also used to generate a linear line, as in Atto488. A plot of the inverse of correlation amplitude, i.e. the number of molecules versus concentration in nM fit a linear line. The unknown concentrations of eGFP::Bcd and eGFP::NLS in the embryos were found from the line equation shown in Fig. S11B,D. For details on the issues on the concentration estimation of posterior domain, see supplementary Materials and Methods.

### SPIM based imaging-FCS

Embryos were imaged on a home build selective plane illumination microscope (SPIM) set up as described previously (Dhasmana et al., 2021; Krieger et al., 2015; Ng et al., 2016). For elaborated details on the configuration, mounting of embryos for SPIM-FCS and processing, see supplementary Materials and Methods section.

### Quantification of eGFP::Bcd, eGFP::Bcd$^{N51A}$, eGFP::Bcd$^{R54A}$, eGFP::Bcd$^{MM}$and eGFP::NLS gradients

Time lapse videos of embryos (eGFP::Bcd and Bicoid mutants with H2b::mCherry background) at n.c. 14 were acquired along the longitudinal plane passing through midline of the embryo. For each embryo, two separate images of 512×512 pixels along the mid sagittal plane covering anterior and posterior domains of the embryo were stitched together. The images were captured at 8 bits/pixel, pixel dwell time of 3 µs, line averaging 4, five *z*-sections of 1 µm each. The conditions captured maximum in-focus peripheral nuclei along the mid-sagittal plane in the Zeiss LSM 710 confocal scanning microscope. The nuclear eGFP intensities along the embryo circumference at n.c. 14 were measured manually by placing an elliptical window in the nuclear centres (Histone::mCherry marked nuclei) that covers maximum nuclear area of all nuclei around the peripheral edge of the embryo in ImageJ.

The measured raw nuclear intensity profile along the circumference of the embryo was background corrected and plotted against the actual length of the embryo. We estimated background using two approaches. First, we simply subtracted the background outside the embryo. However, this is does not account for the illumination variation across the embryo and also possible yolk effects. We also imaged embryos expressing H2b::mCherry but not Bcd::eGFP. For these embryos, we imaged in both 488 nm and 561 nm channels. The 488 nm channel provides an estimate of the background signal for our Bcd::eGFP measurements (similar to Gregor et al., 2007a).

### Modelling of gradient formation

We considered Bcd to be produced within a region close to the anterior, defined by $f(x, x_s)=1$ if $x<x_s$ and $0$ otherwise. We take $x_s=30$ µm, consistent with previous observations of *bcd* mRNA and fits from our Bcd::eGFP measurements. We also allow this to be a fitting parameter in the equations. $D$ is taken from the FCS measurements. We took $\mu=1/50$ min, consistent with eGFP lifetime in the early *Drosophila* embryo (Durrieu et al., 2018). Again, we also allow this to be a fitting parameter in the simulations, but it stays around this bound. Boundary conditions $\partial_x\phi(x=0, t)=0$ and $\partial_x\phi(x=L, t)=0$ were used, where $L=500$ µm represents the embryo length. We also account for the time taken for Bcd to fold (around 45 min). Formulae and parameter details are provided in the supplementary Materials and Methods.

For eGFP::Bcd, the equations are given in the main text. All equations solved in 1D using MATLAB pdepe solver with zero flux boundary conditions at $x=L$. Parameter fitting was carried out as follows. We performed 100 simulations for each model. Each simulation was fitted to a randomly generated concentration profile formed by using the measured mean and s.d. in the concentration at each position; i.e. we fit to a range of profiles that are defined by the experimental error (a form of bootstrapping). We then calculate the mean and s.d. of each fitting parameter. Parameter minimisation was performed using *fminsearch* in Matlab. Code has been deposited in Github (https://github.com/TimSaundersLab). Further details are provided in the supplementary Materials and Methods. Full lists of parameter values and different models considered are provided in the supplementary Materials and Methods.

#### Acknowledgements

We thank the Center for Bioimaging Sciences, Department of Biological Sciences and Microscopy core (Mechanobiology Institute, NUS, Singapore) and CAMDU (University of Warwick) for microscopy facilities. We also thank NDORMS (University of Oxford) for their help with FCS measurements in the revision stages of this manuscript.

#### Competing interests

The authors declare no competing or financial interests.

#### Author contributions

Conceptualization: C.B., T.E.S.; Methodology: T.A., A.V.S.N., N.K., M.F., T.W., T.E.S.; Software: A.V.S.N., T.W.; Validation: A.V.S.N., T.W.; Formal analysis: T.A., C.B., T.E.S.; Investigation: T.A., T.W., T.E.S.; Resources: T.A., N.K., M.F., T.W., T.E.S.; Data curation: T.A., C.B.; Writing - original draft: T.A., T.W., T.E.S.; Writing - review & editing: T.A., A.V.S.N., C.B., N.K., M.F., T.W., T.E.S.; Visualization: T.A., T.E.S.; Supervision: M.F., T.W., T.E.S.; Project administration: T.W., T.E.S.; Funding acquisition: T.W., T.E.S.

#### Funding

This work was funded by the Ministry of Education - Singapore (Tier 3 grant MOE2016-T3-1-005 to T.W. and T.E.S.; Tier 2 grant MOE2018-T2-2-138 to T.E.S.). T.E.S was also supported by a European Molecular Biology Organization Global Investigator award and by start-up support from the University of Warwick. C.B. was funded by the Global Fellows Program of the College of Agriculture and Life Sciences, Cornell University. Open access funding provided by the University of Warwick. Deposited in PMC for immediate release.

#### Data availability

Code has been deposited in Github (https://github.com/TimSaundersLab). A confocal FCS curve fitting resource is available at https://www.dbs.nus.edu.sg/lab/BFL/confocal_FCS.html. An imaging FCS analysis resource is available at https://www.dbs.nus.edu.sg/lab/BFL/imfcs_image_j_plugin.html.

#### Peer review history

The peer review history is available online at https://journals.biologists.com/dev/lookup/doi/10.1242/dev.202128.reviewer-comments.pdf

#### References

**Abu-Arish, A., Porcher, A., Czerwonka, A., Dostatni, N. and Fradin, C.** (2010). High mobility of bicoid captured by fluorescence correlation spectroscopy: implication for the rapid establishment of its gradient. *Biophys. J.* **99**, L33-L35. doi:10.1016/j.bpj.2010.05.031

**Ali-Murthy, Z. and Kornberg, T. B.** (2016). Bicoid gradient formation and function in the Drosophila pre-syncytial blastoderm. *eLife* **5**, e13222. doi:10.7554/eLife.13222

**Barolo, S., Carver, L. A. and Posakony, J. W.** (2000). GFP and β-galactosidase transformation vectors for promoter/enhancer analysis in Drosophila. *BioTechniques* **29**, 726, 728, 730, 732. doi:10.2144/00294bm10

**Briscoe, J. and Small, S.** (2015). Morphogen rules: design principles of gradient-mediated embryo patterning. *Development* **142**, 3996-4009. doi:10.1242/dev.129452

**Burz, D. S., Rivera-Pomar, R., Jackle, H. and Hanes, S. D.** (1998). Cooperative DNA-binding by Bicoid provides a mechanism for threshold-dependent gene activation in the Drosophila embryo. *EMBO J.* **17**, 5998-6009. doi:10.1093/emboj/17.20.5998

**Cai, X., Akber, M., Spirov, A. and Baumgartner, S.** (2017). Cortical movement of Bicoid in early Drosophila embryos is actin- and microtubule-dependent and disagrees with the SDD diffusion model. *PLoS ONE* **12**, e0185443. doi:10.1371/journal.pone.0185443

**Castle, B. T., Howard, S. A. and Odde, D. J.** (2011). Assessment of transport mechanisms underlying the Bicoid morphogen gradient. *Cell Mol. Bioeng.* **4**, 116-121. doi:10.1007/s12195-010-0157-4

**Cho, P. F., Poulin, F., Cho-Park, Y. A., Cho-Park, I. B., Chicoine, J. D., Lasko, P. and Sonenberg, N.** (2005). A new paradigm for translational control: inhibition via 5′-3′ mRNA tethering by Bicoid and the eIF4E cognate 4EHP. *Cell* **121**, 411-423. doi:10.1016/j.cell.2005.02.024

**Dhasmana, D., Veerapathiran, S., Azbazdar, Y., Nelanuthala, A. V. S., Teh, C., Ozhan, G. and Wohland, T.** (2021). Wnt3 is lipidated at conserved cysteine and

serine residues in zebrafish neural tissue. *Front. Cell Dev. Biol.* **9**, 671218. doi:10.3389/fcell.2021.671218
**Donà, E., Barry, J. D., Valentin, G., Quirin, C., Khmelinskii, A., Kunze, A., Durdu, S., Newton, L. R., Fernandez-Minan, A., Huber, W. et al.** (2013). Directional tissue migration through a self-generated chemokine gradient. *Nature* **503**, 285-289. doi:10.1038/nature12635
**Driever, W. and Nüsslein-Volhard, C.** (1988). A gradient of bicoid protein in Drosophila embryos. *Cell* **54**, 83-93. doi:10.1016/0092-8674(88)90182-1
**Drocco, J. A., Grimm, O., Tank, D. W. and Wieschaus, E.** (2011). Measurement and perturbation of morphogen lifetime: effects on gradient shape. *Biophys. J.* **101**, 1807-1815. doi:10.1016/j.bpj.2011.07.025
**Durrieu, L., Kirrmaier, D., Schneidt, T., Kats, I., Raghavan, S., Hufnagel, L., Saunders, T. E. and Knop, M.** (2018). Bicoid gradient formation mechanism and dynamics revealed by protein lifetime analysis. *Mol. Syst. Biol.* **14**, e8355. doi:10.15252/msb.20188355
**Eldar, A., Rosin, D., Shilo, B.-Z. and Barkai, N.** (2003). Self-enhanced ligand degradation underlies robustness of morphogen gradients. *Dev. Cell* **5**, 635-646. doi:10.1016/S1534-5807(03)00292-2
**Fradin, C.** (2017). On the importance of protein diffusion in biological systems: The example of the Bicoid morphogen gradient. *Biochim. Biophys. Acta Proteins Proteom.* **1865**, 1676-1686. doi:10.1016/j.bbapap.2017.09.002
**Gregor, T., Tank, D. W., Wieschaus, E. F. and Bialek, W.** (2007a). Probing the limits to positional information. *Cell* **130**, 153-164. doi:10.1016/j.cell.2007.05.025
**Gregor, T., Wieschaus, E. F., McGregor, A. P., Bialek, W. and Tank, D. W.** (2007b). Stability and nuclear dynamics of the bicoid morphogen gradient. *Cell* **130**, 141-152. doi:10.1016/j.cell.2007.05.026
**Gregor, T., McGregor, A. P. and Wieschaus, E. F.** (2008). Shape and function of the Bicoid morphogen gradient in dipteran species with different sized embryos. *Dev. Biol.* **316**, 350-358. doi:10.1016/j.ydbio.2008.01.039
**Griffin, E. E., Odde, D. J. and Seydoux, G.** (2011). Regulation of the MEX-5 gradient by a spatially segregated kinase/phosphatase cycle. *Cell* **146**, 955-968. doi:10.1016/j.cell.2011.08.012
**Grimm, O. and Wieschaus, E.** (2010). The Bicoid gradient is shaped independently of nuclei. *Development* **137**, 2857-2862. doi:10.1242/dev.052589
**Grimm, O., Coppey, M. and Wieschaus, E.** (2010). Modelling the Bicoid gradient. *Development* **137**, 2253-2264. doi:10.1242/dev.032409
**Hamaratoglu, F., de Lachapelle, A. M., Pyrowolakis, G., Bergmann, S. and Affolter, M.** (2011). Dpp signaling activity requires Pentagone to scale with tissue size in the growing Drosophila wing imaginal disc. *PLoS Biol.* **9**, e1001182. doi:10.1371/journal.pbio.1001182
**Hazelrigg, T., Liu, N., Hong, Y. and Wang, S.** (1998). GFP expression in Drosophila tissues: time requirements for formation of a fluorescent product. *Dev. Biol.* **199**, 245-249. doi:10.1006/dbio.1998.8922
**He, F., Saunders, T. E., Wen, Y., Cheung, D., Jiao, R., ten Wolde, P. R., Howard, M. and Ma, J.** (2010). Shaping a morphogen gradient for positional precision. *Biophys. J.* **99**, 697-707. doi:10.1016/j.bpj.2010.04.073
**Hernandez-Lopez, C., Puliafito, A., Xu, Y., Lu, Z., Di Talia, S. and Vergassola, M.** (2023). Two-fluid dynamics and micron-thin boundary layers shape cytoplasmic flows in early Drosophila embryos. *Proc. Natl. Acad. Sci. U. S. A.* **120**, e2302879120. doi:10.1073/pnas.2302879120
**Ho, J., Tumkaya, T., Aryal, S., Choi, H. and Claridge-Chang, A.** (2019). Moving beyond P values: data analysis with estimation graphics. *Nat. Methods* **16**, 565-566. doi:10.1038/s41592-019-0470-3
**Höfling, F. and Franosch, T.** (2013). Anomalous transport in the crowded world of biological cells. *Rep. Prog. Phys.* **76**, 046602. doi:10.1088/0034-4885/76/4/046602
**Huang, A. and Saunders, T. E.** (2020). A matter of time: formation and interpretation of the Bicoid morphogen gradient. *Curr. Top. Dev. Biol.* **137**, 79-117. doi:10.1016/bs.ctdb.2019.11.016
**Huang, A., Amourda, C., Zhang, S., Tolwinski, N. S. and Saunders, T. E.** (2017). Decoding temporal interpretation of the morphogen Bicoid in the early Drosophila embryo. *eLife* **6**, e26258. doi:10.7554/eLife.26258
**Huang, A., Rupprecht, J.-F. and Saunders, T. E.** (2020). Embryonic geometry underlies phenotypic variation in decanalized conditions. *eLife* **9**, e47380. doi:10.7554/eLife.47380
**Huang, W. Y. C., Cheng, X. and Ferrell, J. E.Jr**. (2022). Cytoplasmic organization promotes protein diffusion in Xenopus extracts. *Nat. Commun.* **13**, 5599. doi:10.1038/s41467-022-33339-0
**Kapusta, P.** (2010). Absolute diffusion coefficients: compilation of reference data for FCS calibration. *PicoQuant*. https://www.academia.edu/16774813/Absolute_diffusion_coefficients_Compilation_of_reference_data_for_FCS_calibration
**Kerszberg, M. and Wolpert, L.** (1998). Mechanisms for positional signalling by morphogen transport: a theoretical study. *J. Theor. Biol.* **191**, 103-114. doi:10.1006/jtbi.1997.0575
**Khmelinskii, A., Keller, P. J., Bartosik, A., Meurer, M., Barry, J. D., Mardin, B. R., Kaufmann, A., Trautmann, S., Wachsmuth, M., Pereira, G. et al.** (2012). Tandem fluorescent protein timers for in vivo analysis of protein dynamics. *Nat. Biotechnol.* **30**, 708-714. doi:10.1038/nbt.2281
**Kicheva, A., Pantazis, P., Bollenbach, T., Kalaidzidis, Y., Bittig, T., Jülicher, F. and González-Gaitán, M.** (2007). Kinetics of morphogen gradient formation. *Science* **315**, 521-525. doi:10.1126/science.1135774
**Kornberg, T. B.** (2014). Cytonemes and the dispersion of morphogens. *Wiley Interdiscip. Rev. Dev. Biol.* **3**, 445-463. doi:10.1002/wdev.151
**Krieger, J. W., Singh, A. P., Bag, N., Garbe, C. S., Saunders, T. E., Langowski, J. and Wohland, T.** (2015). Imaging fluorescence (cross-) correlation spectroscopy in live cells and organisms. *Nat. Protoc.* **10**, 1948-1974. doi:10.1038/nprot.2015.100
**Krzic, U., Gunther, S., Saunders, T. E., Streichan, S. J. and Hufnagel, L.** (2012). Multiview light-sheet microscope for rapid in toto imaging. *Nat. Methods* **9**, 730-733. doi:10.1038/nmeth.2064
**Kuhn, T., Landge, A. N., Mörsdorf, D., Coßmann, J., Gerstenecker, J., Čapek, D., Müller, P. and Gebhardt, J. C. M.** (2022). Single-molecule tracking of Nodal and Lefty in live zebrafish embryos supports hindered diffusion model. *Nat. Commun.* **13**, 6101. doi:10.1038/s41467-022-33704-z
**Lebrecht, D., Foehr, M., Smith, E., Lopes, F. J. P., Vanario-Alonso, C. E., Reinitz, J., Burz, D. S. and Hanes, S. D.** (2005). Bicoid cooperative DNA binding is critical for embryonic patterning in Drosophila. *Proc. Natl. Acad. Sci. USA* **102**, 13176-13181. doi:10.1073/pnas.0506462102
**Ling, J., Umezawa, K. Y., Scott, T. and Small, S.** (2019). Bicoid-dependent activation of the target gene hunchback requires a two-motif sequence code in a specific basal promoter. *Mol. Cell* **75**, 1178-1187.e1174. doi:10.1016/j.molcel.2019.06.038
**Lipkow, K. and Odde, D. J.** (2008). Model for protein concentration gradients in the cytoplasm. *Cell. Mol. Bioeng.* **1**, 84-92. doi:10.1007/s12195-008-0008-8
**Little, S. C., Tkačik, G., Kneeland, T. B., Wieschaus, E. F. and Gregor, T.** (2011). The formation of the Bicoid morphogen gradient requires protein movement from anteriorly localized mRNA. *PLoS Biol.* **9**, e1000596. doi:10.1371/journal.pbio.1000596
**Lord, N. D., Carte, A. N., Abitua, P. B. and Schier, A. F.** (2021). The pattern of nodal morphogen signaling is shaped by co-receptor expression. *eLife* **10**, e54894. doi:10.7554/eLife.54894.sa2
**Ma, X., Yuan, D., Diepold, K., Scarborough, T. and Ma, J.** (1996). The Drosophila morphogenetic protein Bicoid binds DNA cooperatively. *Development* **122**, 1195-1206. doi:10.1242/dev.122.4.1195
**MacDonald, P. M.** (2005). Translational repression by Bicoid: competition for the cap. *Cell* **121**, 321-322. doi:10.1016/j.cell.2005.04.018
**Mir, M., Reimer, A., Haines, J. E., Li, X.-Y., Stadler, M., Garcia, H., Eisen, M. B. and Darzacq, X.** (2017). Dense Bicoid hubs accentuate binding along the morphogen gradient. *Genes Dev.* **31**, 1784-1794. doi:10.1101/gad.305078.117
**Mir, M., Stadler, M. R., Ortiz, S. A., Hannon, C. E., Harrison, M. M., Darzacq, X. and Eisen, M. B.** (2018). Dynamic multifactor hubs interact transiently with sites of active transcription in Drosophila embryos. *eLife* **7**, e40497. doi:10.7554/eLife.40497
**Müller, P., Rogers, K. W., Jordan, B. M., Lee, J. S., Robson, D., Ramanathan, S. and Schier, A. F.** (2012). Differential diffusivity of Nodal and Lefty underlies a reaction-diffusion patterning system. *Science* **336**, 721-724. doi:10.1126/science.1221920
**Müller, P., Rogers, K. W., Yu, S. R., Brand, M. and Schier, A. F.** (2013). Morphogen transport. *Development* **140**, 1621-1638. doi:10.1242/dev.083519
**Ng, X. W., Teh, C., Korzh, V. and Wohland, T.** (2016). The secreted signaling protein wnt3 is associated with membrane domains in vivo: a SPIM-FCS study. *Biophys. J.* **111**, 418-429. doi:10.1016/j.bpj.2016.06.021
**Niessing, D., Dostatni, N., Jackle, H. and Rivera-Pomar, R.** (1999). Sequence interval within the PEST motif of Bicoid is important for translational repression of caudal mRNA in the anterior region of the Drosophila embryo. *EMBO J.* **18**, 1966-1973. doi:10.1093/emboj/18.7.1966
**Niessing, D., Driever, W., Sprenger, F., Taubert, H., Jäckle, H. and Rivera-Pomar, R.** (2000). Homeodomain position 54 specifies transcriptional versus translational control by Bicoid. *Mol. Cell* **5**, 395-401. doi:10.1016/S1097-2765(00)80434-7
**Niessing, D., Blanke, S. and Jäckle, H.** (2002). Bicoid associates with the 5′-cap-bound complex of caudal mRNA and represses translation. *Genes Dev.* **16**, 2576-2582. doi:10.1101/gad.240002
**Patterson, G. H., Knobel, S. M., Sharif, W. D., Kain, S. R. and Piston, D. W.** (1997). Use of the green fluorescent protein and its mutants in quantitative fluorescence microscopy. *Biophys. J.* **73**, 2782-2790. doi:10.1016/S0006-3495(97)78307-3
**Porcher, A., Abu-Arish, A., Huart, S., Roelens, B., Fradin, C. and Dostatni, N.** (2010). The time to measure positional information: maternal hunchback is required for the synchrony of the Bicoid transcriptional response at the onset of zygotic transcription. *Development* **137**, 2795-2804. doi:10.1242/dev.051300
**Romanova-Michaelides, M., Hadjivasiliou, Z., Aguilar-Hidalgo, D., Basagiannis, D., Seum, C., Dubois, M., Jülicher, F. and Gonzalez-Gaitan, M.** (2022). Morphogen gradient scaling by recycling of intracellular Dpp. *Nature* **602**, 287-293. doi:10.1038/s41586-021-04346-w
**Roy, S., Huang, H., Liu, S. and Kornberg, T. B.** (2014). Cytoneme-mediated contact-dependent transport of the Drosophila decapentaplegic signaling protein. *Science* **343**, 1244624. doi:10.1126/science.1244624

**Saunders, T. E. and Howard, M.** (2009). Morphogen profiles can be optimized to buffer against noise. *Phys. Rev. E Stat. Nonlin. Soft Matter Phys.* **80**, 041902. doi:10.1103/PhysRevE.80.041902

**Sigaut, L., Pearson, J. E., Colman-Lerner, A. and Ponce Dawson, S.** (2014). Messages do diffuse faster than messengers: reconciling disparate estimates of the morphogen bicoid diffusion coefficient. *PLoS Comput. Biol.* **10**, e1003629. doi:10.1371/journal.pcbi.1003629

**Singh, A. P., Wu, P., Ryabichko, S., Raimundo, J., Swan, M., Wieschaus, E., Gregor, T. and Toettcher, J. E.** (2022). Optogenetic control of the Bicoid morphogen reveals fast and slow modes of gap gene regulation. *Cell Rep.* **38**, 110543. doi:10.1016/j.celrep.2022.110543

**Spirov, A., Fahmy, K., Schneider, M., Frei, E., Noll, M. and Baumgartner, S.** (2009). Formation of the bicoid morphogen gradient: an mRNA gradient dictates the protein gradient. *Development* **136**, 605-614. doi:10.1242/dev.031195

**Stanganello, E., Hagemann, A. I. H., Mattes, B., Sinner, C., Meyen, D., Weber, S., Schug, A., Raz, E. and Scholpp, S.** (2015). Filopodia-based Wnt transport during vertebrate tissue patterning. *Nat. Commun.* **6**, 5846. doi:10.1038/ncomms6846

**Stapornwongkul, K. S. and Vincent, J.-P.** (2021). Generation of extracellular morphogen gradients: the case for diffusion. *Nat. Rev. Genet.* **22**, 393-411. doi:10.1038/s41576-021-00342-y

**Stapornwongkul, K. S., de Gennes, M., Cocconi, L., Salbreux, G. and Vincent, J.-P.** (2020). Patterning and growth control in vivo by an engineered GFP gradient. *Science* **370**, 321-327. doi:10.1126/science.abb8205

**Thummel, C. S. and Pirrotta, V.** (1992). Technical notes: new pCasper P-element vectors. *Drosophila Information Service* **71**, 150.

**Veerapathiran, S., Teh, C., Zhu, S., Kartigayen, I., Korzh, V., Matsudaira, P. T. and Wohland, T.** (2020). Wnt3 distribution in the zebrafish brain is determined by expression, diffusion and multiple molecular interactions. *eLife* **9**, e59489. doi:10.7554/eLife.59489

**Vukojević, V., Papadopoulos, D. K., Terenius, L., Gehring, W. J. and Rigler, R.** (2010). Quantitative study of synthetic Hox transcription factor-DNA interactions in live cells. *Proc. Natl. Acad. Sci. USA* **107**, 4093-4098. doi:10.1073/pnas.0914612107

**Wang, Y., Wang, X., Wohland, T. and Sampath, K.** (2016). Extracellular interactions and ligand degradation shape the nodal morphogen gradient. *eLife* **5**, e13879. doi:10.7554/eLife.13879

**Wartlick, O., Kicheva, A. and Gonzalez-Gaitan, M.** (2009). Morphogen gradient formation. *Cold Spring Harb. Perspect. Biol.* **1**, a001255. doi:10.1101/cshperspect.a001255

**Yu, S. R., Burkhardt, M., Nowak, M., Ries, J., Petrášek, Z., Scholpp, S., Schwille, P. and Brand, M.** (2009). Fgf8 morphogen gradient forms by a source-sink mechanism with freely diffusing molecules. *Nature* **461**, 533-536. doi:10.1038/nature08391

**Yuan, D., Ma, X. and Ma, J.** (1996). Sequences outside the homeodomain of bicoid are required for protein-protein interaction. *J. Biol. Chem.* **271**, 21660-21665. doi:10.1074/jbc.271.35.21660

**Zhou, S., Lo, W.-C., Suhalim, J. L., Digman, M. A., Gratton, E., Nie, Q. and Lander, A. D.** (2012). Free extracellular diffusion creates the Dpp morphogen gradient of the Drosophila wing disc. *Curr. Biol.* **22**, 668-675. doi:10.1016/j.cub.2012.02.065

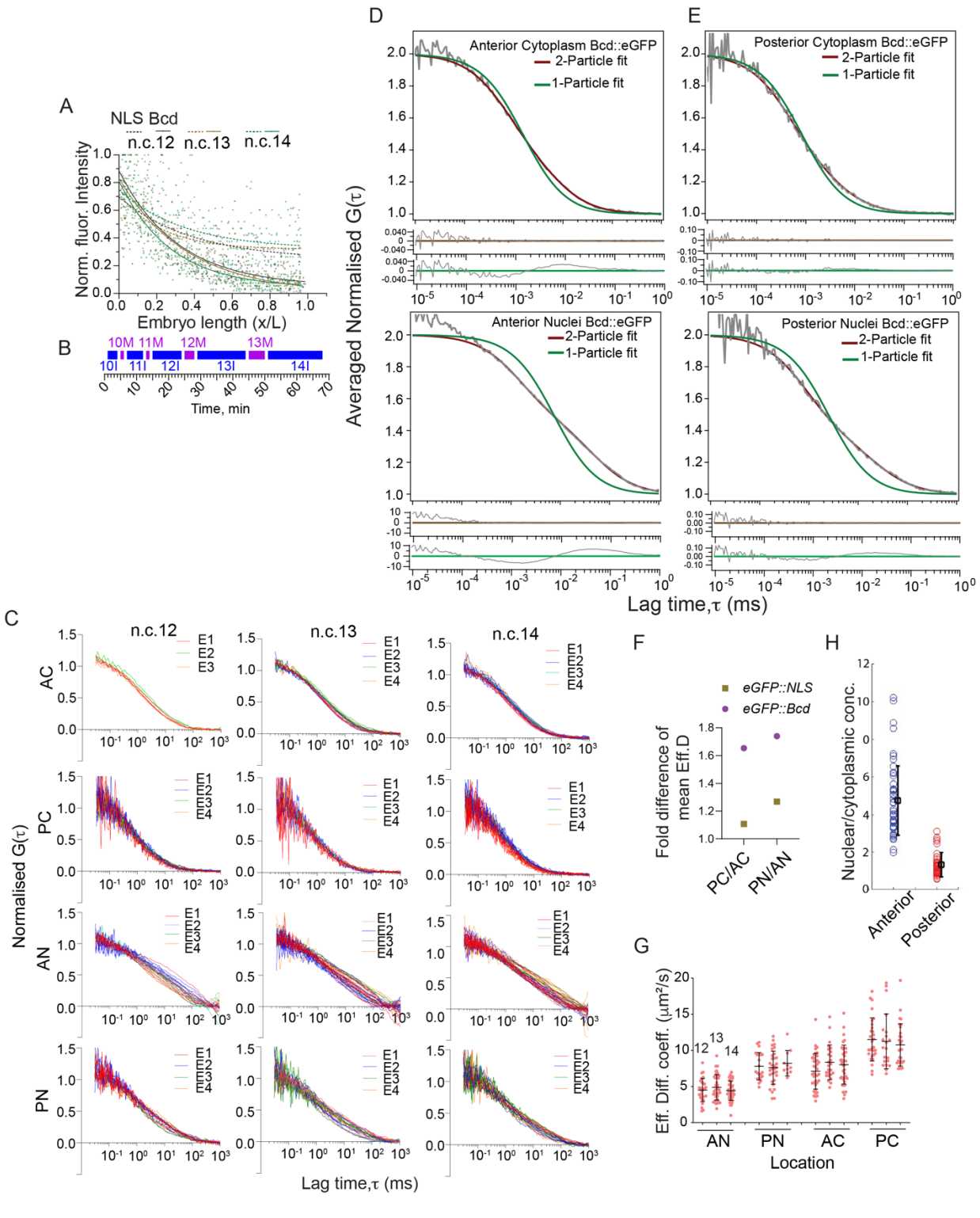


**Fig. S1. FCS and fitting of eGFP::Bcd (related to Figure 1)**

(A) Comparison of the gradient profiles of eGFP::Bcd and eGFP::NLS plotted with normalised fluorescence intensities in Y-axis and the normalised embryo length (x/L). Dots show individual nuclear intensities, and the solid lines are fits to exponential profiles. (B) Time profile of the early embryo from n.c. 10 to 14 at 25ºC. I indicates interphase, and M, mitosis. (C) Normalised ACF curves of eGFP::Bcd in the cytoplasmic and nuclear compartments of anterior (Anterior Cytoplasm, AC, Anterior Nuclei, AN) and posterior (Posterior Cytoplasm, PC, Posterior Nuclei, PN) in nuclear cycle (n.c.) 12, 13, and 14 interphases. (D, E) Comparison of ACF curves (grey) with residues fitted using 3D 1-particle and 2-particle diffusion model in the anterior cytoplasm (D), nuclei (D') and posterior cytoplasm (E), nucleus (E'). (F) Effective diffusion coefficients of nuclear and cytoplasmic locations of the anterior and posterior domains are compared for individual n.c. 12, 13, and 14. (G) Fold change in the mean diffusion coefficient across the embryo for the cytoplasmic and nuclear compartments. Comparison for eGFP::Bcd (circles) and eGFP::NLS (squares) are shown. (H) Ratio of measured apparent concentration (from ACF curve amplitude) in the nuclei and cytoplasm of anterior and posterior compartments. Note the posterior concentration is approximated as the signal is very low in the posterior compartment.

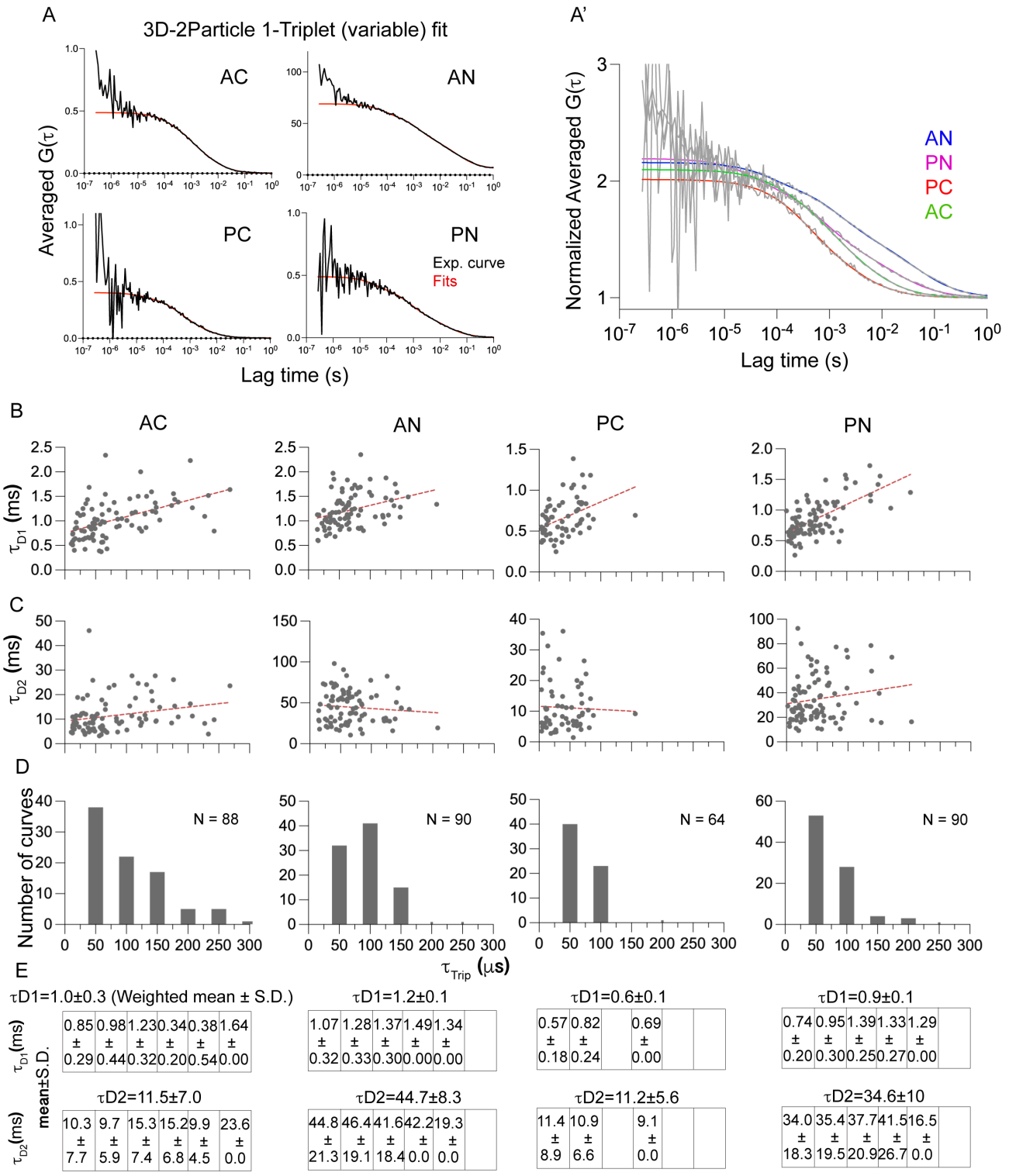


**Fig. S2. Fitting and analysis of eGFP::Bcd with 3D 2-particle and variable triplet (related to Fig. 1)**

(A) ACF curves of eGFP:Bcd (black) in the cytoplasm and nuclear compartments of anterior and posterior domains from nuclear cycles 12-14 fitted with 3D 2-Particle 1-triplet model with triplet states are allowed to vary. The normalised curves are shown in A'. The ACF curves are fitted from $10^{-5}$s to 1s as the curves below $10^{-5}$ are noisy. (B,C) Scatter plot showing $\tau_{D1}$ (B) and $\tau_{D2}$ (C) distribution with respect to the $\tau_{Triplet}$ values for each curves. ACF curves from n.c.12, 13 and 14 are considered together in this analysis as there are no variations in D values observed across these nuclear cycles. (D) Distribution of ACF curves every 50μs of $\tau_{Triplet}$ values ranged from 0 to 300μs. N represents total number of curves. (E) The mean and S.D. of $\tau_{D1}$ and $\tau_{D2}$ values of binned ACF curves are in D. Note: Maximum number of curves have $\tau_{Triplet}$ value of <100μs in all four cases of ACF curves. Weighted means and S.D. of $\tau_{D1}$ and $\tau_{D2}$ are also shown in E that matches with the $\tau_{D1}$ and $\tau_{D2}$ values of 2-Particle fits without considering triplet in Table 2 and 3.

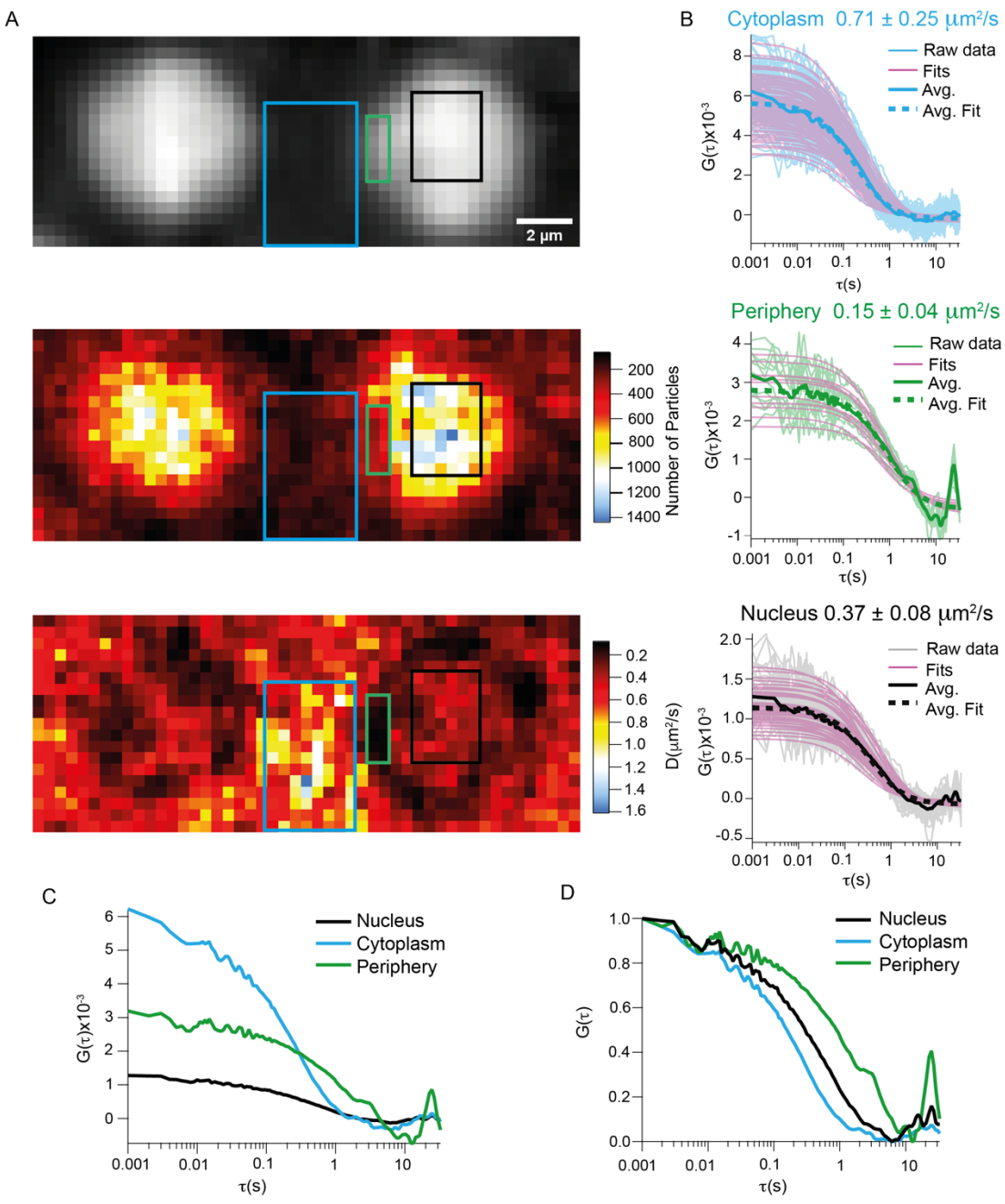


**Fig. S3. SPIM-based Imaging-FCS on eGFP::Bicoid**

(A) Intensity sum projection (top), number of particles (N, middle), and diffusion coefficient (D, bottom) maps for eGFP::Bcd in the anterior margin of the embryo during n.c. 13. The spatial maps show Bcd's relative localisation and dynamics in and around the nuclei. As seen from the N map, Bcd mostly localises inside the nucleus, followed by the nuclear periphery, and its concentration in the cytoplasm is relatively low. Conversely, the D map shows that Bcd diffuses faster in the cytoplasm than in the nucleus and is relatively slow at the nuclear periphery. (B) Individual ACFs from pixels, fits and the average ACFs for different ROIs representing the cytoplasm (cyan n = 104), nuclear periphery (green n = 12) and inside the nucleus (black n = 48). Based on the fit values obtained, the diffusion coefficients in different spaces vary as $D_{cytoplasm} > D_{nucleus} > D_{periphery}$. (C) Comparison between the average ACFs from the nucleus, cytoplasm, and nuclear periphery ROIs. The ACF amplitude is highest for the cytoplasm, followed by the nuclear periphery and is the lowest for the ACF from the nucleus. As the amplitudes of the ACFs are inversely proportional to the number of particles, the ACFs show that $N_{nucleus} > N_{periphery} > N_{cytoplasm}$. (D) Comparison between the normalised average ACFs from the nucleus, cytoplasm, and nuclear periphery ROIs.

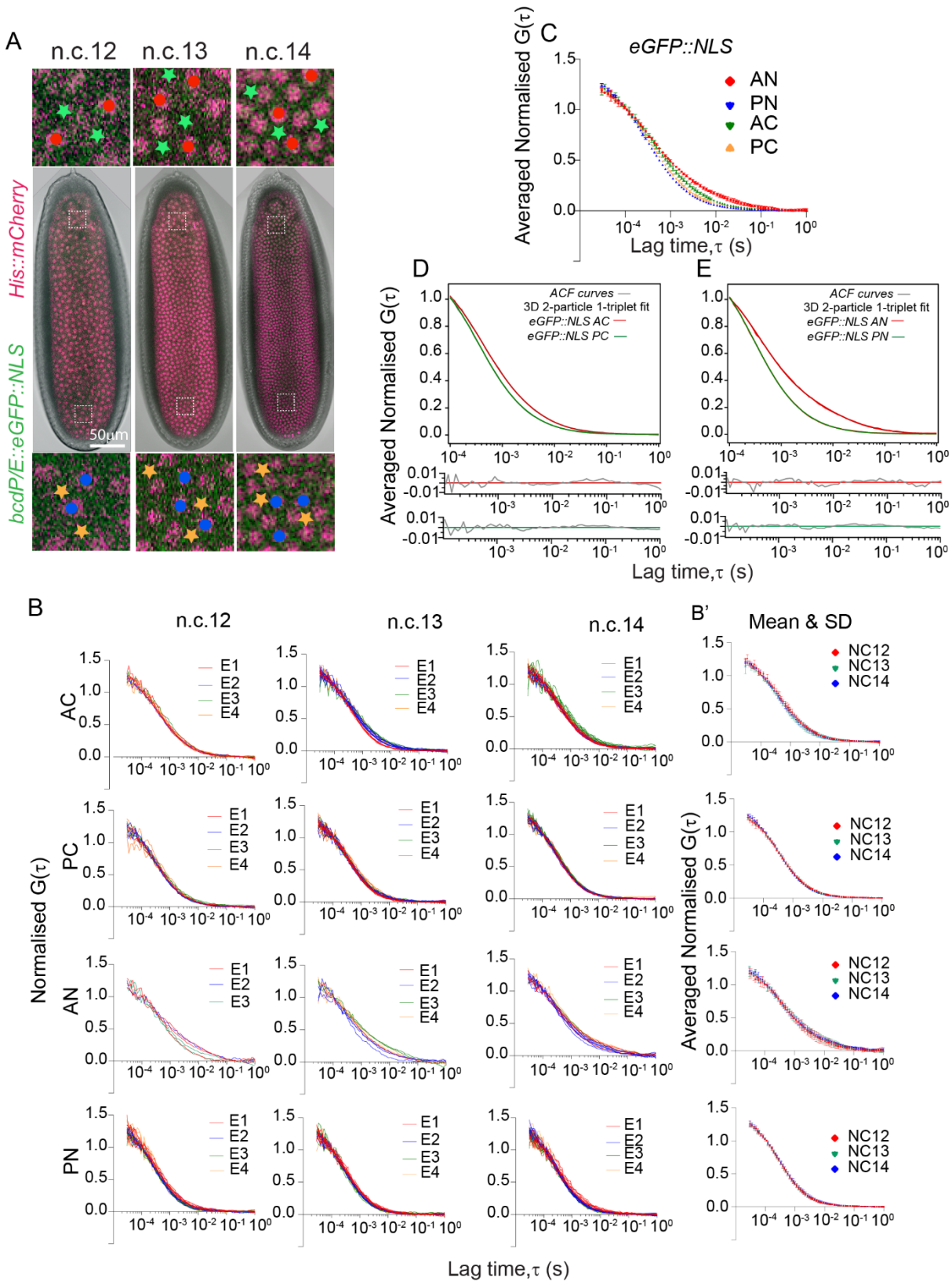


**Fig. S4. FCS and fitting of eGFP::NLS (related to Figure 2)**

(A) *Drosophila* blastoderm showing the interphase periods of n.c. 12, 13 and 14. Nuclei (mCherry::His2Aν, red) and eGFP::NLS (green). Dots and stars indicate cytoplasmic and nuclear regions, respectively, where FCS measurements are carried out in the anterior (red) and posterior (green). (B-B') Normalised ACF curves with mean and S.D. of eGFP::NLS in cytoplasmic and nuclear compartments of the n.c. 12,13, and 14 interphases. (C) Comparison of normalised, averaged ACF curves with mean and S.D. of eGFP::NLS in cytoplasmic and nuclear compartments in n.c. 12,13, and 14 interphases. (D-E) ACF curves (grey) with residues fitted with 3D 2-particle 1-triplet diffusion model for cytoplasm (D) and nuclei (E).

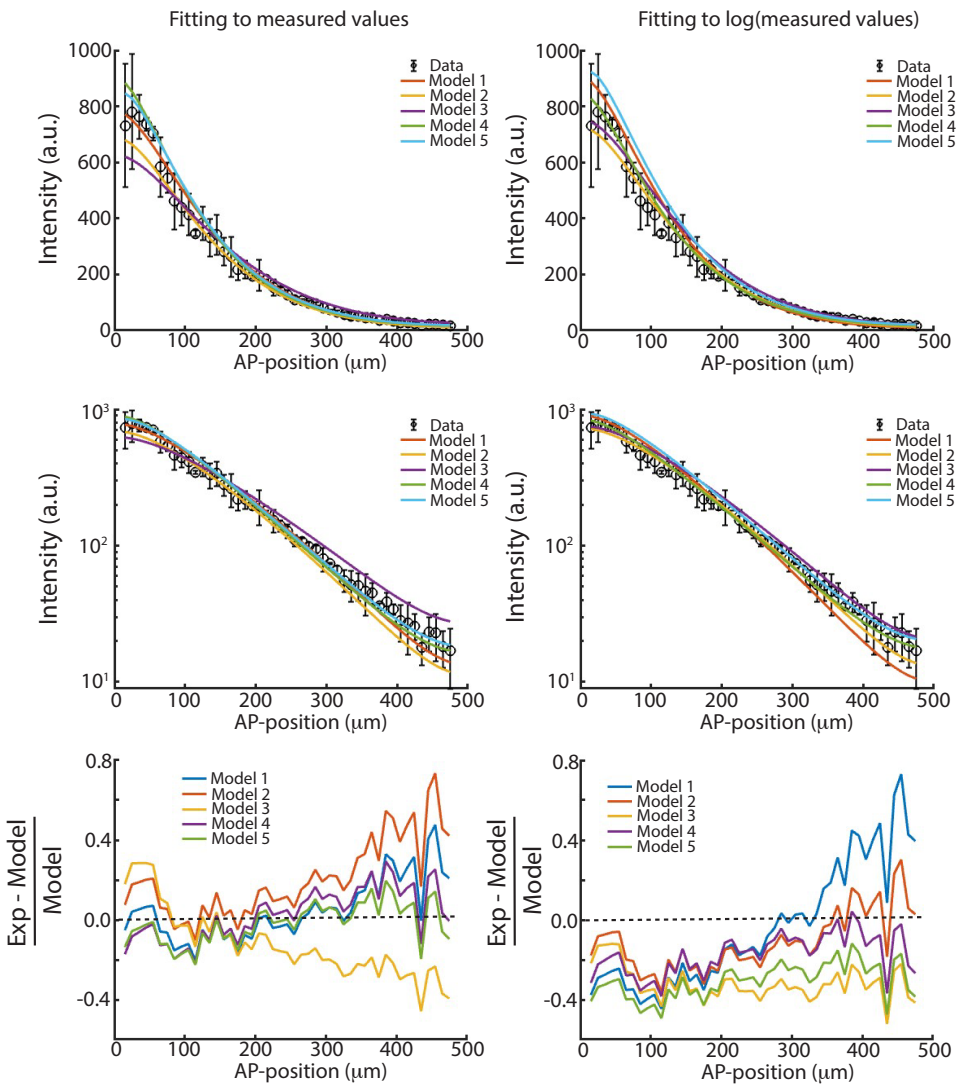


**Fig. S5. Model fitting (related to Figure 3)**

Model fits as described in the Supplementary Information to the experimental Bcd::eGFP profile. Left column represents fitting to background-subtracted intensity values. Right column represents fitting to log(background-subtracted intensity values). Experimental data shown as mean and s.d.. Top row: fit to data on linear scale. Middle row: fit to data on logarithmic intensity scale. Bottom row: Quality of fit across the embryo axis. Perfect fit shown by dashed black line.

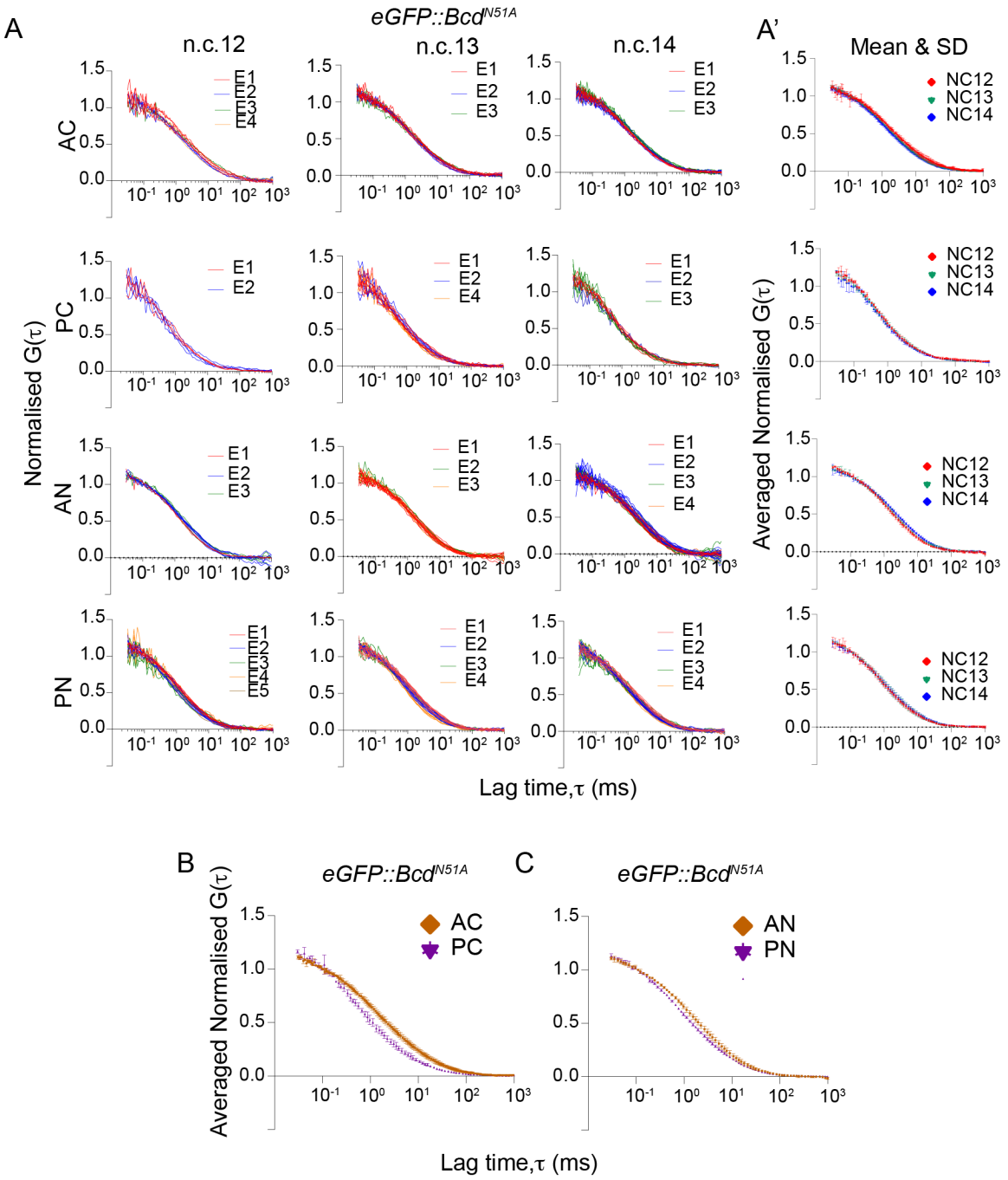


**Fig. S6. FCS and fitting of eGFP:Bcd$^{N51A}$ (related to Figure 4)**

(A-A') Normalised ACF curves with mean and S.D. of eGFP::Bcd$^{N51A}$ in the cytoplasmic and nuclear compartments of the n.c. 12,13, and 14 interphases. (B-C) Normalised average ACF curves of eGFP::bcd$^{N51A}$ in the cytoplasmic (B) and nuclear (C) locations of the anterior and posterior domains of the embryo.

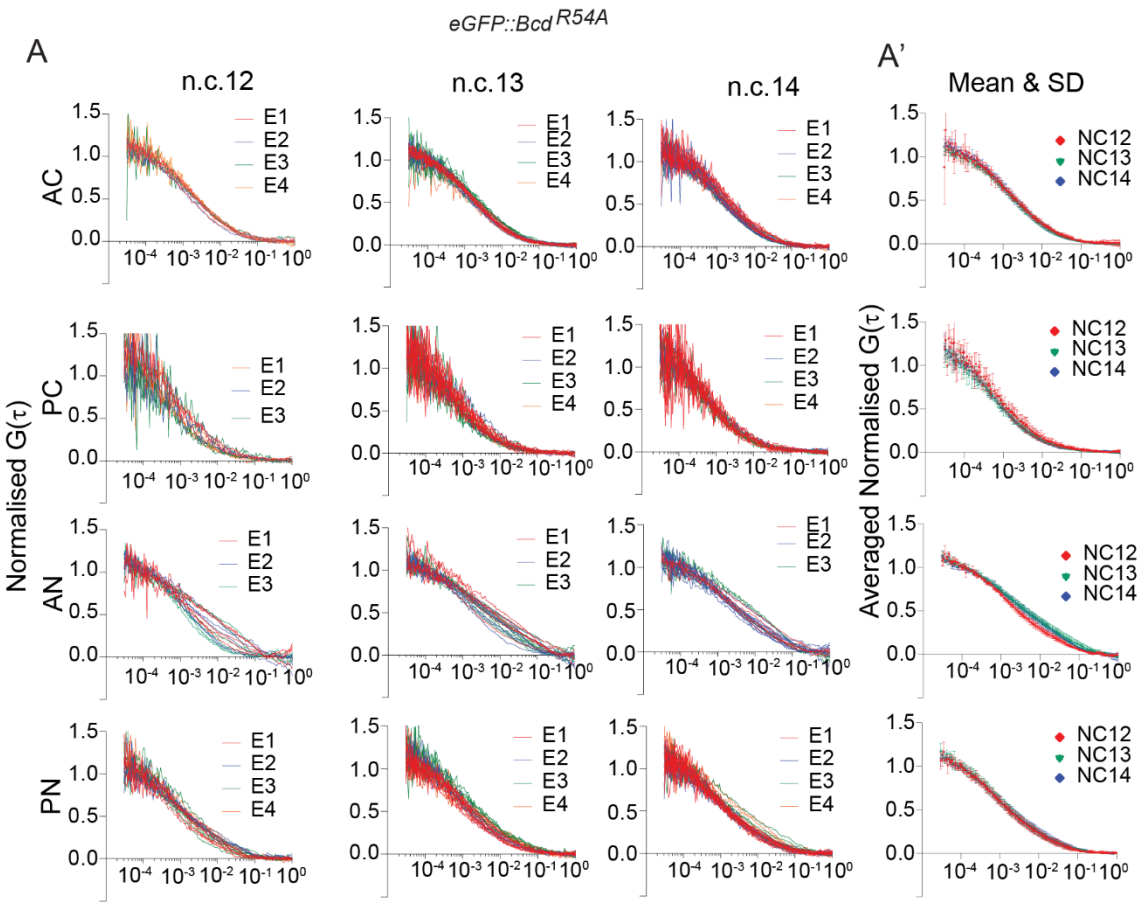


**Fig. S7. Dynamics of eGFP::Bcd$^{R54A}$ (related to Figure 4)**

(A) Normalised ACF curves with mean and S.D. of eGFP::Bcd$^{R54A}$ in the cytoplasmic and nuclear compartments of the n.c. 12,13, and 14 interphases. Normalised ACF curves from multiple embryos are shown. Lag times from $10^{-4}$ sec to 1sec are shown for visual clarity. (A') Normalised and averaged autocorrelation ACF curves with mean and S.D. of eGFP::Bcd$^{R54A}$ in the cytoplasmic and nuclear compartments of the n.c. 12,13, and 14 interphases.

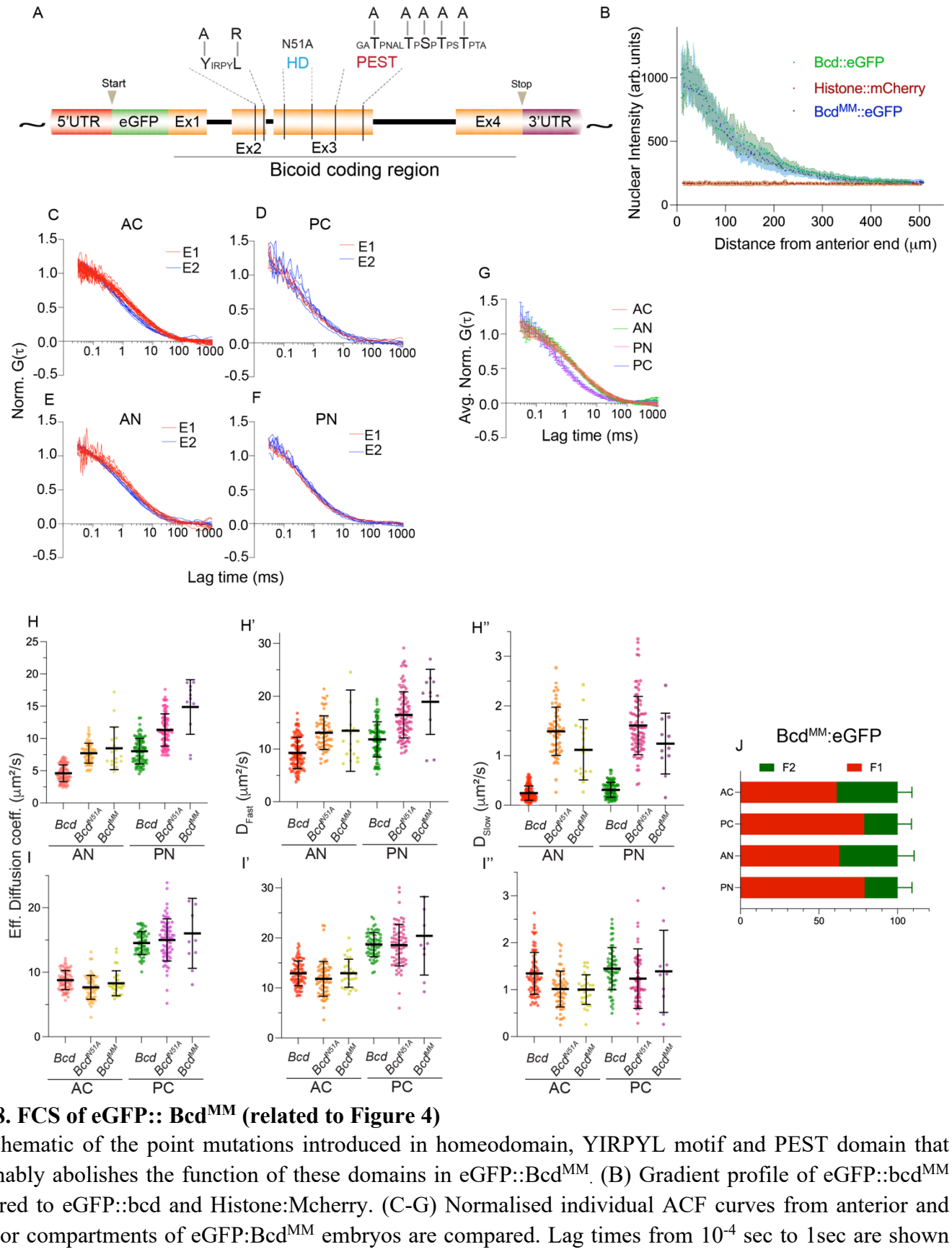


**Fig. S8. FCS of eGFP:: Bcd$^{MM}$ (related to Figure 4)**

(A) Schematic of the point mutations introduced in homeodomain, YIRPYL motif and PEST domain that presumably abolishes the function of these domains in eGFP::Bcd$^{MM}$. (B) Gradient profile of eGFP::bcd$^{MM}$ compared to eGFP::bcd and Histone:Mcherry. (C-G) Normalised individual ACF curves from anterior and posterior compartments of eGFP:Bcd$^{MM}$ embryos are compared. Lag times from $10^{-4}$ sec to 1sec are shown for visual clarity. (H-I) Scatter plots of the effective diffusion (H,I), $D_{fast}$ (H',I') and $D_{slow}$ (H''-I'') values compared among eGFP:Bcd, eGFP:Bcd$^{N51A}$ and eGFP:Bcd$^{MM}$ . (G) Bar plots comparing the fractions of slow and fast components of the eGFP:bcd$^{MM}$.

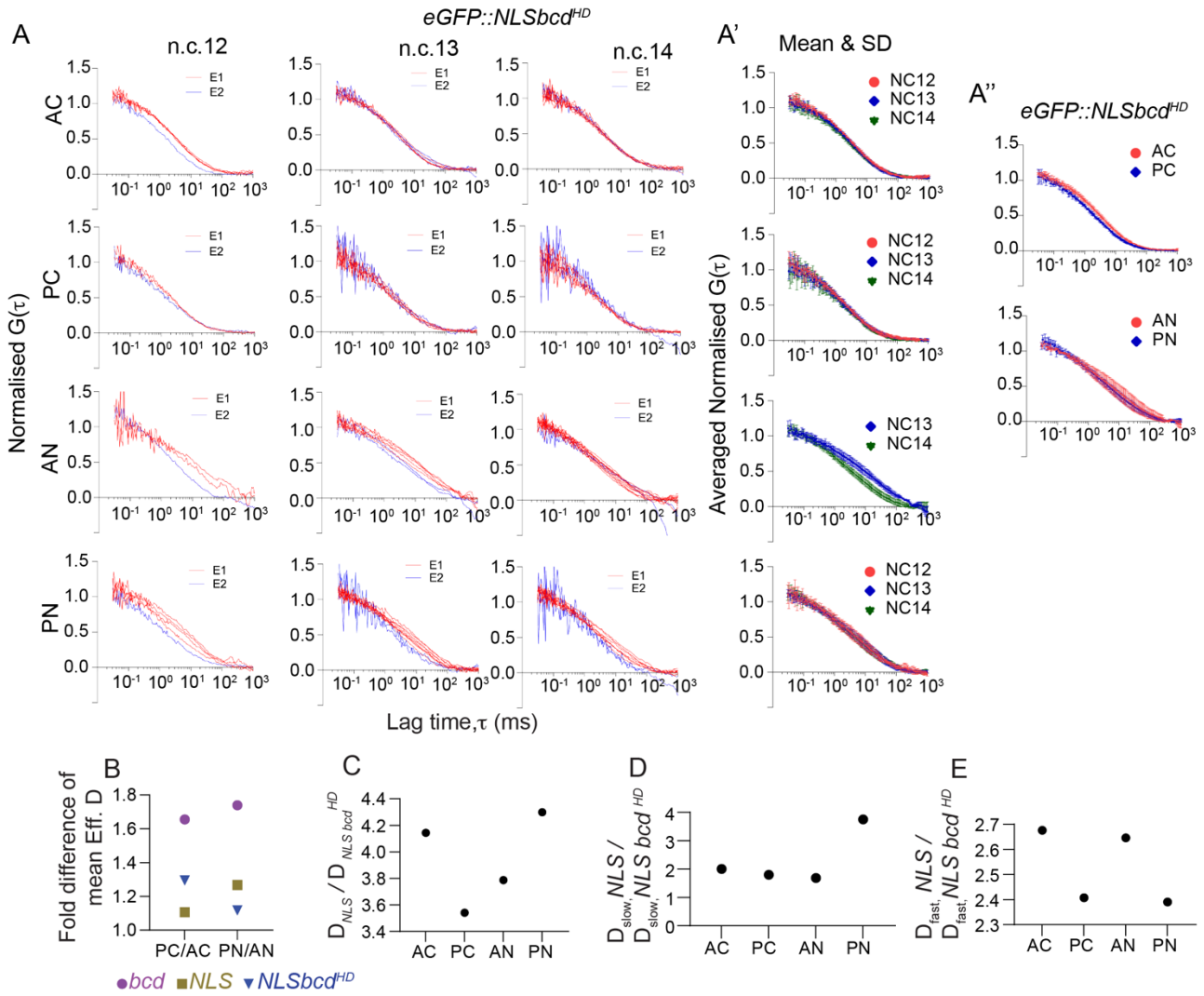


**Fig. S9. FCS of eGFP::NLSbcd$^{HD}$ (related to Figure 5)**

(A-A') Normalised ACF curves with mean and S.D. of eGFP::NLSbcd$^{HD}$ embryos in the cytoplasmic and nuclear compartments of the n.c. 12,13, and 14 interphases. Normalised ACF curves from two embryos (right) are compared. Lag times from $10^{-4}$ sec to 1sec are shown for visual clarity. (A'') Qualitative comparison of normalised ACF curves with mean and S.D. of eGFP::NLSbcd$^{HD}$ in the cytoplasmic and nuclear compartments of the n.c. 12,13, and 14 interphases. (B-E) Change in relative diffusivity of eGFP::NLSbcd$^{HD}$ compared with eGFP::NLS at different locations within the embryo.

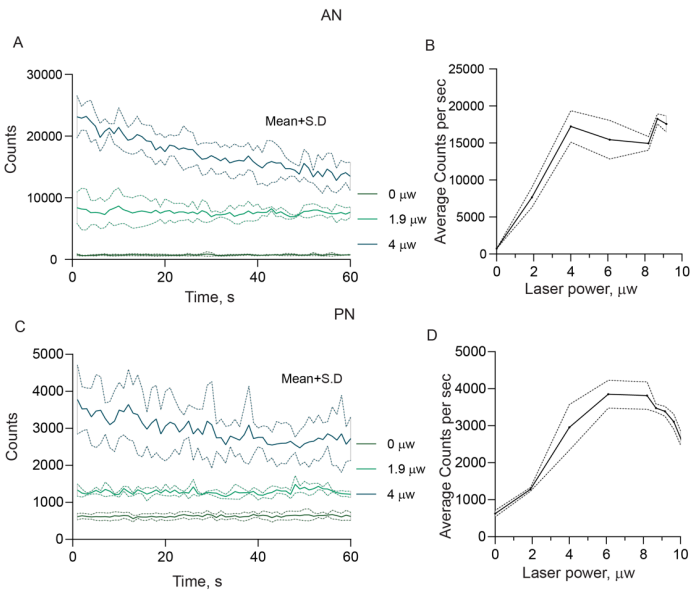


**Fig. S10. Laser power optimisation**

(A, C) line plot showing the time trace of the eGFP:Bcd in the anterior (A) and posterior nuclei (C). Mean (solid line) and SD (dotted line) of the time trace are shown for laser powers 0, 1.9 and 4µw. (laser power was measured before the objective) (B, D) Mean counts per sec increases with laser power and gets saturated above laser power of 4µw due to photobleaching.

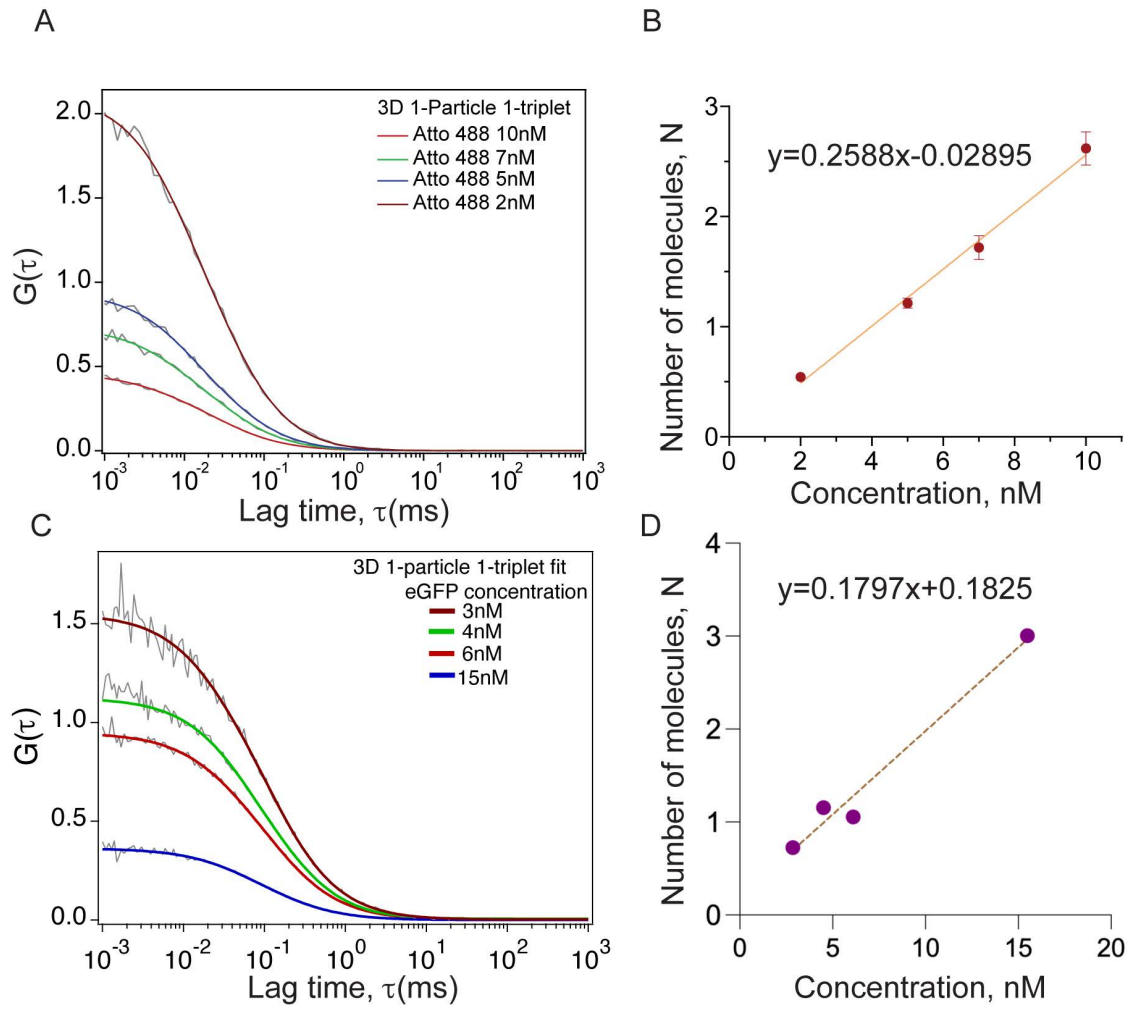


**Fig. S11 (related to Figs. 1,2 and S1).** Calibration of effective volume to estimate the concentration
(A,C) Normalised ACF curves (grey) of Atto-488 (A) and of eGFP (C) of different concentration and the 1-particle 1-triplet fits. (B,D) linear increase in number of molecules in the confocal volume upon increasing the concentrations of Atto-488 and eGFP invitro. The standard curve shows negligible changes in both cases. Equation from Atto488 is used for concentration measurements.

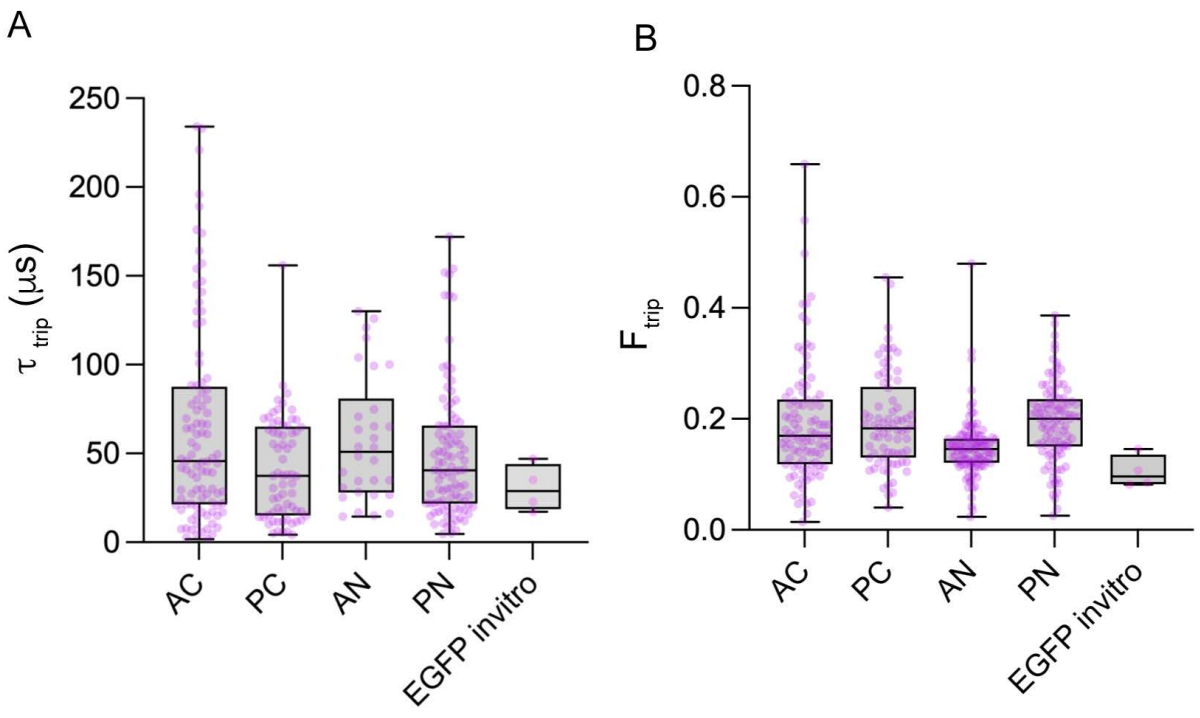


**Fig. S12 (related to S2). Estimation of triplet lifetime, $t_{triplet}$ and its fraction ($F_{triplet}$)**
(A) Box-whisker plot showing the values of the characteristic times of photophysical processes, $t_{triplet}$, from multiple ACF curves measured from 4 embryos, across all compartments. Triplet information from eGFP in PBS is also included. The fraction ($F_{trip}$)is given in B. AC- anterior cytoplasm, PC-posterior cytoplasm, AN-anterior nuclei, and PN-posterior nuclei.

**Table S1. Comparison of parameter values of 1-particle and 2-particle fits of eGFP::Bcd with fixed G(0) and G(μ) (related to Fig. 1 and Fig. S1).**

| | 1-Particle | | | 2-Particle | | | | | | | |
|---|---|---|---|---|---|---|---|---|---|---|---|
| Nuclear cycle | TauD(ms) | D(μm2/s) | Reduced Chi^2 | TauD1(ms) | D1(μm2/s) | TauD2(ms) | D2(μm2/s) | F1 (%) | F2(%) | Eff.D (μm2/s) | Chi^2 |
| **Anterior Cytoplasm** | | | | | | | | | | | |
| n.c.12 | 1.8±0.2 | 5.7±0.7 | 5.1 | 0.9±0.2 | 11.8±2.6 | 9.3±2.7 | 1.1±0.3 | 69±11 | 31±11 | 8.3±1.1 | 1.1 |
| n.c.13 | 2.0±0.6 | 5.4±1.4 | 4.1 | 1.0±0.3 | 10.8±2.9 | 10.8±4.6 | 1.0±0.3 | 69±1 | 31±1 | 7.8±2.1 | 0.8 |
| n.c.14 | 1.7±0.4 | 6.1±1.3 | 3.7 | 0.7±0.2 | 14.6±4.1 | 7.3±2.5 | 1.5±0.5 | 62±6 | 38±6 | 9.5±2.2 | 1.0 |
| **Posterior Cytoplasm** | | | | | | | | | | | |
| n.c.12 | 1.1±0.2 | 9.3±1.4 | 1.0 | 0.6±0.2 | 16.5±4.7 | 7.3±3.5 | 1.6±0.5 | 76±8 | 24±8 | 12.7±2.8 | 0.4 |
| n.c.13 | 1.0±0.2 | 9.7±1.6 | 1.7 | 0.6±0.1 | 16.2±3.5 | 8.0±3.4 | 1.4±0.5 | 78±7 | 22±7 | 12.8±2.3 | 0.6 |
| n.c.14 | 1.0±0.1 | 10.5±0.8 | 3.6 | 0.6±0.0 | 17.6±1.4 | 8.6±2.9 | 1.3±0.3 | 78±6 | 22±6 | 14.0±0.6 | 0.7 |
| **Anterior Nuclei** | | | | | | | | | | | |
| n.c.12 | 7.9±3.7 | 1.4±0.5 | 20.9 | 1.2±0.3 | 8.7±1.9 | 44.1±17.0 | 0.3±0.1 | 48±5 | 52±5 | 4.3±1.1 | 1.5 |
| n.c.13 | 8.8±2.6 | 1.2±0.3 | 21.9 | 1.4±0.1 | 7.0±0.7 | 57.9±15.4 | 0.2±0.1 | 52±3 | 48±3 | 3.7±0.5 | 1.4 |
| n.c.14 | 11.8±5.8 | 1.0±0.3 | 30.2 | 1.6±0.4 | 6.6±1.4 | 76.5±26.0 | 0.1±0.0 | 50±4 | 50±4 | 3.4±0.9 | 2.5 |
| **Posterior Nuclei** | | | | | | | | | | | |
| n.c.12 | 3.1±1.6 | 3.8±1.4 | 25.3 | 1.0±0.5 | 11.4±3.9 | 47.9±13.0 | 0.4±0.1 | 65±2 | 35±2 | 7.6±2.7 | 1.3 |
| n.c.13 | 3.0±0.2 | 3.6±1.0 | 37.7 | 0.8±0.2 | 12.8±2.3 | 36.6±13.2 | 0.3±0.1 | 63±3 | 37±3 | 8.3±1.7 | 2.0 |
| n.c.14 | 3.9±1.0 | 2.7±0.6 | 34.6 | 1.0±0.2 | 10.0±2.2 | 47.9±11.7 | 0.2±0.1 | 63±1 | 37±1 | 6.3±1.4 | 1.3 |

**Table S2. Comparison of parameter values of cytoplasmic eGFP:Bcd and eGFP:NLS diffusion fit using 3D 2-particle diffusion model.** *(The duration of each cytoplasmic measurement are 60 secs in all cases)*

| eGFP::Bcd AC : 3D-Diffusion 2-particle model | | | | | | | | |
|---|---|---|---|---|---|---|---|---|
| N.C. | Embryo No. (no. of ACF curves) | $TauD_1$ (ms) | D1 ($\mu m^2/s$) | Fraction ($F_1$%) | $TauD_2$ (ms) | $D_2$ ($\mu m^2/s$) | Fraction ($F_2$%) | Eff.Diff. ($\mu m^2/s$) |
| 12 | 1(4),2(4),3(6),4(4) | 0.8±0.1 | 13.2±1.1 | 66±4 | 8.5±1.7 | 1.3±0.2 | 34±4 | 9.1±0.8 |
| 13 | 1(9),2(8),3(4),4(5) | 0.8±0.1 | 12.8±0.8 | 66±5 | 10.0±1.4 | 1.2±0.2 | 34±3 | 8.7±1.1 |
| 14 | 1(15),2(12),3(12),4(7) | 0.8±0.1 | 12.9±1.1 | 64±5 | 7.9±2.1 | 1.4±0.3 | 36±5 | 8.7±1.1 |
| **eGFP::Bcd PC : 3D-Diffusion 2-particle model** | | | | | | | | |
| 12 | 1(3),2(3),3(3),4(4) | 0.5±0.0 | 19.2±1.6 | 78±3 | 8.5±1.7 | 1.3±0.2 | 22±3 | 15.3±1.6 |
| 13 | 1(4),2(6),3(7),4(3) | 0.6±0.0 | 18.4±0.7 | 77±5 | 7.7±1.3 | 1.3±0.2 | 23±5 | 14.4±0.9 |
| 14 | 1(7),2(7),3(4),4(4) | 0.6±0.0 | 19.0±1.2 | 79±3 | 9.8±1.6 | 1.2±0.1 | 21±3 | 15.2±1.2 |
| **eGFP::NLS AC : 3D-Diffusion 2-particle model** | | | | | | | | |
| 12 | 1(4),2(2),3(3),4(2) | 0.4±0.0 | 25.5±1.7 | 85±2 | 6.8±1.5 | 1.7±0.2 | 15±2 | 21.8±0.9 |
| 13 | 1(4),2(4),3(7),2(4) | 0.4±0.0 | 27.9±3.6 | 84±6 | 6.4±2.6 | 2.0±0.6 | 16±6 | 22.8±1.0 |
| 14 | 1(8),2(7),3(5),4(6) | 0.4±0.0 | 26.4±1.2 | 84±7 | 5.6±2.1 | 2.3±0.5 | 16±7 | 22.5±0.8 |
| **eGFP::NLS PC : 3D-Diffusion 2-particle model** | | | | | | | | |
| 12 | 1(3),2(4),3(3),4(1) | 0.3±0.0 | 28.1±3.2 | 91±0 | 6.4±1.7 | 2.1±1.3 | 9±0 | 26.1±2.6 |
| 13 | 1(3),2(4),3(6),4(5) | 0.4±0.0 | 27.0±1.3 | 92±2 | 5.3±1.8 | 2.5±0.4 | 8±2 | 25.0±1.4 |
| 14 | 1(1),2(4),3(4),4(6) | 0.4±0.0 | 26.4±2.6 | 94±1 | 6.9±2.8 | 2.3±0.6 | 6±1 | 25.1±2.2 |

**Table S3. Comparison of parameter values of nuclear eGFP:Bcd and eGFP:NLS diffusion fit using 3D 2-particle diffusion model** *(The duration of each nuclear measurement is 20-40 secs.)*

| eGFP::Bcd AN : 3D-Diffusion 2-particle model | | | | | | | | |
|---|---|---|---|---|---|---|---|---|
| N.C. | Embryo No. (no. of ACF curves) | TauD1 (ms) | D1 ($\mu m^2/s$) | Fraction ($F_1$%) | TauD2 (ms) | D2 ($\mu m^2/s$) | Fraction ($F_2$%) | Eff.Diff. ($\mu m^2/s$) |
| 12 | 1(6),2(8),3(5),4(3) | 1.1±0.1 | 9.7±1.3 | 50±4 | 43.0±6.2 | 0.3±0.1 | 50±4 | 4.9±0.5 |
| 13 | 1(9),2(11),3(6),4(8) | 1.2±0.1 | 9.3±0.5 | 49±3 | 66.4±15.6 | 0.3±0.0 | 51±3 | 4.6±0.5 |
| 14 | 1(13),2(10),3(11),4(10) | 1.2±0.1 | 9.0±0.8 | 49±4 | 65.2±7.6 | 0.2±0.0 | 51±4 | 4.5±0.5 |
| **eGFP::Bcd PN : 3D-Diffusion 2-particle model** | | | | | | | | |
| 12 | 1(8), 2(4), 3(6), 4(5) | 0.9±0.1 | 11.9±1.5 | 64±3 | 36.0±9.4 | 0.4±0.1 | 36±3 | 7.7±1.1 |
| 13 | 1(9), 2(9), 3(10), 4(5) | 0.8±0.1 | 13.1±1.3 | 61±1 | 38.3±5 | 0.4±0.1 | 39±1 | 8.1±0.9 |
| 14 | 1(5), 2(8), 3(9), 4(7) | 0.9±0.1 | 11.9±1.3 | 63±2 | 42.2±11 | 0.3±0.1 | 37±2 | 7.5±0.7 |
| **eGFP:NLS AN : 3D-Diffusion 2-particle model** | | | | | | | | |
| 12 | 1(2),2(1),3(2) | 0.4±0.0 | 26.1±0.5 | 84±0 | 6.6±3.3 | 1.7±0.8 | 16±0 | 21.8±0.5 |
| 13 | 1(1),2(4),3(2),4(3) | 0.4±0.0 | 26.1±2.6 | 79±6 | 12.2±2.3 | 0.9±0.3 | 21±6 | 20.4±1.2 |
| 14 | 1(3),2(6),3(1),4(4) | 0.4±0.0 | 27.1±2.0 | 80±5 | 15.7±5.4 | 0.9±0.2 | 20±5 | 21.7±2.6 |
| **eGFP::NLS PN : 3D-Diffusion 2-particle model** | | | | | | | | |
| 12 | 1(5),2(3),3(7),4(2) | 0.3±0.0 | 28.2±2.2 | 95±1 | 9.6±5.0 | 2.1±1.4 | 5±1 | 26.9±2.2 |
| 13 | 1(4),2(5),3(3),4(8) | 0.3±0.0 | 30.3±2.8 | 95±1 | 15.5±9.9 | 1.2±0.3 | 5±1 | 28.9±3.0 |
| 14 | 1(4),2(8),3(7),4(6) | 0.3±0.0 | 28.3±2.8 | 95±3 | 14.8±8.3 | 1.3±0.5 | 5±3 | 26.9±2.9 |

**Table S4. Comparison of parameter values of eGFP::Bcd$^{N51A}$ and eGFP::Bcd$^{R54A}$ diffusion fit using 3D 2-particle diffusion model.**

| N.C. | Embryo No. (no. of ACF curves) | TauD$_1$ (ms) | D1 ($\mu m^2/s$) | Fraction ($F_1$%) | TauD$_2$ (ms) | D$_2$ ($\mu m^2/s$) | Fraction ($F_2$%) | Eff.Diff. ($\mu m^2/s$) |
|---|---|---|---|---|---|---|---|---|
| **eGFP::Bcd$^{N51A}$ AN: 3D-Diffusion 2-particle model (30s each measurement)** | | | | | | | | |
| 12 | 1(3),2(6),3(4) | 0.7±0.1 | 16.1±3.8 | 53±3 | 5.3±0.9 | 2.0±0.4 | 47±3 | 9.3±1.5 |
| 13 | 1(6),2(6),4(3) | 0.8±0.1 | 13.5±2.4 | 56±1 | 6.6±0.7 | 1.6±0.2 | 44±1 | 8.1±1.7 |
| 14 | 1(11),2(6),3(8),4(10) | 0.8±0.0 | 13.0±1.0 | 52±1 | 8.0±1.2 | 1.4±0.1 | 48±1 | 7.4±0.7 |
| **eGFP::Bcd$^{N51A}$ PN: 3D-Diffusion 2-particle model (30s each measurement)** | | | | | | | | |
| 12 | 1(6),2(7),3(3),4(3),5(4) | 0.7±0.0 | 15.8±1.5 | 69±5 | 7.0±1.2 | 1.7±0.4 | 31±5 | 11.0±1.3 |
| 13 | 1(11),2(10),3(5), 4(5),5(6) | 0.7±0.1 | 16.0±2.2 | 67±5 | 7.0±1.8 | 1.5±0.2 | 33±5 | 11.0±2.0 |
| 14 | 1(7),2(12),3(8),4(6),5(9) | 0.6±0.1 | 17.0±3.2 | 64±6 | 7.0±1.2 | 1.6±0.2 | 36±6 | 11.0±2.0 |
| **eGFP::Bcd$^{N51A}$ AC: 3D-Diffusion 2-particle model (60s each measurement)** | | | | | | | | |
| 12 | 1(4),2(2),3(1),4(2) | 1.0±0.2 | 10.7±2.7 | 64±6 | 14.1±4.3 | 0.8±0.3 | 36±6 | 7.1±1.3 |
| 13 | 1(6),2(6),3(5),4(6) | 1.0±0.3 | 10.7±2.4 | 64±3 | 13.4±4.3 | 0.9±0.3 | 36±3 | 7.0±1.4 |
| 14 | 1(6),2(7),3(8),4(8) | 0.9±0.3 | 12.3±2.7 | 64±2 | 11.8±5.4 | 1.0±0.3 | 36±2 | 8.0±1.7 |
| **eGFP::Bcd$^{N51A}$ PC: 3D-Diffusion 2-particle model (60s each measurement)** | | | | | | | | |
| 12 | 1(4),2(2),3(4) | 0.6±0.1 | 16.9±0.6 | 79±7 | 9.5±1.7 | 1.2±0.3 | 20±7 | 13.5±1.6 |
| 13 | 1(6),2(6),3(4),4(8),5(7) | 0.6±0.0 | 18.5±2.8 | 79±3 | 9.7±2.5 | 1.3±0.5 | 21±3 | 14.7±2.2 |
| 14 | 1(6),2(4),3(6),4(6) | 0.6±0.0 | 18.3±1.1 | 83±6 | 11.3±1.7 | 1.1±0.3 | 17±6 | 15.2±1.2 |
| **eGFP::Bcd$^{R54A}$ AN: 3D-Diffusion 2-particle model (30s each measurement)** | | | | | | | | |
| 12 | 1(5),2(2),3(5) | 1.2±0.2 | 9.3±0.4 | 59±3 | 37.0±8.0 | 0.4±0.1 | 41±3 | 5.5±0.0 |
| 13 | 1(5),2(4),3(9) | 1.4±0.2 | 8.1±1.3 | 55±1 | 57.8±15.0 | 0.3±0.1 | 45±1 | 4.5±0.7 |
| 14 | 1(9),2(12),3(7) | 1.3±0.2 | 8.5±1.6 | 55±2 | 40.1±10.0 | 0.4±0.1 | 45±2 | 4.8±1.1 |
| **eGFP::Bcd$^{R54A}$ PN: 3D-Diffusion 2-particle model (30s each measurement)** | | | | | | | | |
| 12 | 1(5),2(3),3(7) | 0.7±0.1 | 14.4±3.0 | 70±5 | 19.0±5.8 | 0.7±0.2 | 30±5 | 10.2±1.9 |
| 13 | 1(9),2(5),3(7) | 0.7±0.0 | 15.2±1.0 | 70±2 | 16.0±1.0 | 0.7±0.1 | 30±2 | 10.7±0.7 |
| 14 | 1(13),2(8),3(9) | 0.7±0.0 | 16.0±1.0 | 69±1 | 18.0±4.0 | 0.7±0.1 | 31±1 | 11.1±0.6 |
| **eGFP::Bcd$^{R54A}$ AC: 3D-Diffusion 2-particle model (60s each measurement)** | | | | | | | | |
| 12 | 1(5),2(3),3(2),4(2) | 0.9±0.1 | 11.4±1.7 | 66±4 | 10.5±1.6 | 1.0±0.1 | 34±4 | 7.8±1.2 |
| 13 | 1(10),2(7),3(8),4(5) | 1.0±0.2 | 11.3±1.8 | 66±3 | 10.0±3.0 | 1.1±0.3 | 34±3 | 7.7±1.3 |
| 14 | 1(10),2(13),3(3),4(11) | 0.9±0.1 | 11.8±0.7 | 67±7 | 9.7±2.0 | 1.2±0.2 | 33±7 | 8.2±0.2 |
| **eGFP::Bcd$^{R54A}$ PC: 3D-Diffusion 2-particle model (60s each measurement)** | | | | | | | | |
| 12 | 1(4),2(4),3(3),4(4) | 0.8±0.2 | 13.8±2.4 | 84±6 | 21.3±5.0 | 0.6±0.1 | 16±6 | 12.5±1.5 |
| 13 | 1(10),2(3),3(8),4(7) | 0.8±0.1 | 13.8±2.6 | 86±2 | 22.0±5.9 | 0.7±0.2 | 14±2 | 11.8±2.3 |
| 14 | 1(7),2(3),3(7),4(4) | 0.6±0.1 | 17.6±2.9 | 83±5 | 15.0±10.7 | 1.0±0.5 | 17±5 | 14.2±1.9 |

**Table S5. Comparison of parameter values of eGFP::bcd$^{MM}$ diffusion fit using 3D -2-particle diffusion model.**

| N.C. | Embryo No. (no. of ACF curves) | TauD$_1$ (ms) | D1 ($\mu m^2/s$) | Fraction ($F_1$%) | TauD$_2$ (ms) | D$_2$ ($\mu m^2/s$) | Fraction ($F_2$%) | Eff.Diff. ($\mu m^2/s$) |
|---|---|---|---|---|---|---|---|---|
| **eGFP:: bcd$^{MM}$ AN : 3D-Diffusion 2-particle model** | | | | | | | | |
| 12-14 | 1(9), 2(8) | 0.8±0.3 | 13.5±6.6 | 63±10 | 10.8±6.3 | 1.2±0.5 | 37±10 | 8.5±3.3 |
| **eGFP:: bcd$^{MM}$ PN : 3D-Diffusion 2-particle model** | | | | | | | | |
| 12-14 | 1(3), 2(8) | 0.4±0.2 | 20.0±5.2 | 78±9 | 6.2±2.6 | 1.3±0.5 | 22±9 | 15.7±3.5 |
| **eGFP:: bcd$^{MM}$ AC : 3D-Diffusion 2-particle model** | | | | | | | | |
| 12-14 | 1(21), 2(9) | 0.7±0.2 | 13.0±2.8 | 61±9 | 8.5±2.4 | 1.0±0.3 | 39±9 | 8.3±2.0 |
| **eGFP:: bcd$^{MM}$ PC : 3D-Diffusion 2-particle model** | | | | | | | | |
| 12-14 | 1(3), 2(7) | 0.4±0.1 | 22.6±7.2 | 78±9 | 6.3±3.9 | 1.5±0.8 | 22±9 | 16.9±4.9 |

**Table S6. Comparison of parameter values of eGFP::NLSbcd$^{HD}$ diffusion fit using 3D -2-particle diffusion model.**

| N.C. | Embryo No. (no. of ACF curves) | TauD$_1$ (ms) | D1 ($\mu m^2/s$) | Fraction ($F_1$%) | TauD$_2$ (ms) | D$_2$ ($\mu m^2/s$) | Fraction ($F_2$%) | Eff.Diff. ($\mu m^2/s$) |
|---|---|---|---|---|---|---|---|---|
| **eGFP::NLSbcd$^{HD}$ AN : 3D-Diffusion 2-particle model (30s each measurement)** | | | | | | | | |
| 12 | 1(2), 2(1) | 2.3±0.1 | 4.3±0.2 | 49±1 | 55.6±33.3 | 0.2±0.1 | 51±1 | 2.2±0.2 |
| 13 | 1(10), 2(2) | 1.2±0.3 | 9.0±2.2 | 52±13 | 64.3±53.8 | 0.3±0.3 | 48±13 | 4.7±1.5 |
| 14 | 1(12), 3(2) | 0.8±0.3 | 13.3±4.3 | 53±11 | 19.0±8.8 | 0.6±0.3 | 47±11 | 7.2±2.2 |
| **eGFP::NLSbcd$^{HD}$ PN : 3D-Diffusion 2-particle model (30s each measurement)** | | | | | | | | |
| 12 | 1(5), 2(1) | 0.7±0.1 | 14.8±2.7 | 44±13 | 19.3±5.9 | 0.6±0.2 | 56±13 | 6.7±1.2 |
| 13 | 1(10), 2(2) | 0.8±0.3 | 14.0±4.6 | 51±16 | 18.2±6.1 | 0.6±0.2 | 49±16 | 7.3±2.6 |
| 14 | 1(7), 2(2) | 1.3±0.3 | 8.5±2.4 | 54±7 | 25.2±9.8 | 0.4±0.0 | 46±7 | 5.1±0.2 |
| **eGFP::NLSbcd$^{HD}$ AC : 3D-Diffusion 2-particle model (60s each measurement)** | | | | | | | | |
| 12 | 1(4), 2(1) | 1.0±0.3 | 10.6±2.5 | 46±13 | 8.5±2.4 | 1.3±0.4 | 54±12 | 5.3±0.3 |
| 13 | 1(7), 2(2) | 0.8±0.3 | 14.0±4.4 | 39±8 | 7.3±2.3 | 1.4±0.3 | 61±8 | 6.2±1.6 |
| 14 | 1(7), 2(2) | 1.0±0.2 | 10.7±2.4 | 50±5 | 8.2±0.9 | 1.2±0.1 | 50±4 | 6.0±1.0 |
| **eGFP::NLSbcd$^{HD}$ PC : 3D-Diffusion 2-particle model (60s each measurement)** | | | | | | | | |
| 12 | 1(3), 2(1) | 0.9±0.0 | 10.7±0.8 | 57±0 | 7.8±1.4 | 1.3±0.2 | 43±0 | 6.7±0.4 |
| 13 | 1(6), 2(2) | 1.0±0.2 | 10.3±2.0 | 59±7 | 12.6±9.1 | 1.0±0.5 | 41±7 | 6.4±1.0 |
| 14 | 1(9), 2(2) | 1.0±0.3 | 11.4±3.8 | 59±10 | 9.2±3.7 | 1.2±0.4 | 41±10 | 7.2±2.2 |

**Table S7. Table of models considered with fitting parameters.**

| Model | Brief Description | Fixed Parameters | Fitted parameters | Equations |
|---|---|---|---|---|
| **1** | SDD | $\nu = 1/50 mins^{-1}$ | $D = 2.9 \pm 0.1 \mu m^2 s^{-1}$<br>$\mu = 1/49 \pm 1/98\ mins^{-1}$<br>$J = 86 \pm 3\ \mu m^{-2} s^{-1}$ | [1-3] |
| **2** | SDD with source domain | $\nu = 1/50 mins^{-1}$ | $D = 2.8 \pm 0.2 \mu m^2 s^{-1}$<br>$\mu = 1/48 \pm 1/96\ mins^{-1}$<br>$J = 3.1 \pm 0.1\ \mu m^{-3} s^{-1}$<br>$x_0 = 28 \pm 2 \mu m$ | [4] |
| **3** | 2-component with no spatial dependence | $\nu = 1/50 mins^{-1}$<br>$D_{slow} = 1 \mu m^2 s^{-1}$<br>$D_{fast} = 12 \mu m^2 s^{-1}$ | $\alpha = 0.02 \pm 0.004 s^{-1}$<br>$\beta = 0.07 \pm 0.01 s^{-1}$<br>$J = 2.9 \pm 0.6 \mu m^{-3} s^{-1}$<br>$\mu = 0.0003 \pm 0.0001 s^{-1}$<br>$x_0 = 28 \pm 2 \mu m$ | [5] |
| **4** | 2-component with spatial variation only in diffusion coefficients | $\nu = 1/50 mins^{-1}$<br>$D_{1,ant} = 12 \mu m^2 s^{-1}$<br>$D_{1,pos} = 18 \mu m^2 s^{-1}$<br>$D_{2,ant} = 0.5 \mu m^2 s^{-1}$<br>$D_{2,pos} = 1 \mu m^2 s^{-1}$ | $\alpha = 0.08 \pm 0.03 s^{-1}$<br>$\beta = 0.03 \pm 0.01 s^{-1}$<br>$J = 9.1 \pm 2.5 \mu m^{-3} s^{-1}$<br>$\mu = 0.0006 \pm 0.0002 s^{-1}$<br>$x_0 = 27 \pm 4 \mu m$ | [5-6] |
| **5** | 2-component with spatial dependence in diffusion and $\beta$ | $\nu = 1/50 mins^{-1}$<br>$D_{1,ant} = 12 \mu m^2 s^{-1}$<br>$D_{1,pos} = 18 \mu m^2 s^{-1}$<br>$D_{2,ant} = 0.5 \mu m^2 s^{-1}$<br>$D_{2,pos} = 1 \mu m^2 s^{-1}$ | $\alpha = 0.11 \pm 0.01 s^{-1}$<br>$\beta = 0.04 \pm 0.01 s^{-1}$<br>$J = 7.5 \pm 1.4 \mu m^{-3} s^{-1}$<br>$\mu = 0.0006 \pm 0.0001 s^{-1}$<br>$x_0 = 31 \pm 3 \mu m$<br>$x_1 = 208 \pm 30\ \mu m$ | [5-7] |

# Supplementary Materials and Methods

## Additional FCS Calibration Information

*Calibration of FCS measurements:*

We calibrated eccentricity of the confocal volume, κ before each round of measurements using the reference dye Atto-488 (Atto-Tec) that has a diffusion coefficient 400 $\mu m^2/s$ at room temperature (Kapusta, 2010). The effective volume of calibration ($V_{eff}$, from picoquant) was found to be 0.25±0.04fl and the value of κ was found to be 5.6±0.9. The value for κ was fixed at 5.6.

## Additional details on FCS curve Fitting

The 3D model involving diffusion of 2 species was selected as it provided a good fit determined through quality of the residuals of each plot (Abu-Arish et al., 2010). Photophysical processes, *e.g*., triplet transitions (Atto488) or photoisomerisation and protonation kinetics (eGFP) at short times (Widengren et al., 1999) are a concern when estimating accurate diffusion times. The error rate in the measurement of the diffusion time becomes worse if the characteristic times of photophysical processes are large enough to overlap with the diffusion time. Further, since the total fluorescence of eGFP:Bcd in the anterior and posterior cytoplasm is lower compared to the nuclei, the noise in these curves further limits the distinction between photophysics and diffusion, reducing the accuracy of the determined $\tau_D$ values.

Therefore, we fitted our FCS curves with different time ranges to include or exclude the photophysical processes at short times. A lag time range of 0.001ms to 1s was considered for fits including photophysics (Figure S2) and 0.1 ms to 1 s for fits excluding photophysics (Table 2 and 3). The photophysical parameters, denoted for simplicity as $\tau_{trip}$ for the characteristic time and $F_{trip}$ for the fraction, were allowed to vary. The distribution of $\tau_{D1}$ and $\tau_{D2}$ values with respect to their individual ttrip values are plotted and weighted means are calculated (Fig. S2B-E). Our estimation reveals comparable photophysics parameters values across the A-P axis (Fig. S12). The majority of the $\tau_{t\ riplet}$ values range from 30 to 100µs comparable to the characteristic times of eGFP measured previously (Haupts et al., 1998; Jimenez-Banzo et al., 2008). The fraction ranges from 0.15 to 0.22 (Fig. S12). The data with anomalies due to photobleaching or sudden jumps in the intensities due to movement of the nucleus during measurements, were excluded from evaluation.

## Additional details on the concentration estimation of eGFP:Bcd

*Determination of bicoid concentration in the posterior domain of the embryo*

The eGFP::Bcd concentration in the posterior domain of the embryo become very low. Determining the accurate eGFP:Bcd concentration is a challenge. In the Anterior-posterior gradient profile, the quantification of the eGFP:Bcd nuclear intensity compared to that of the His::mcherry autofluorescence measured using 488 laser line reveals the signal is equivalent to the background noise in the posterior domain of the eGFP:Bcd embryo (Figure S13A). Further upon measurement of background noise using FCS we found the counts are ~4000-8500 per second in the cytoplasm and nuclear compartments of anterior and posterior domains. The signal is stronger over noise in the anterior nuclei (~60000cps) and cytoplasm (~10000cps) of the Bcd::eGFP embryos (Figure S13B). Therefore, it is reasonable to assume that the number of the molecules (N) in the anterior domain is $N = 1/G(0)$. In the case of posterior domain, both nuclear and cytoplasm counts are within ~10000 and therefore direct determination of the number of molecules from G(0) is complicated (Figure S13B). In the posterior nuclei, the signal to noise is better than the cytoplasm as suggested by the G(0) which above that of anterior nuclei (Figure S13C). For posterior cytoplasm, the concentration is estimated in figure 2A from the curves that are measured just below the midline of the embryo where the signal-to-noise is better than the posterior most. On the other hand, ACF curves of the background noise (H2b::mcherry) is uncorrelated whereas the bcd::eGFP in the nuclei and cytoplasm of the posterior domain are autocorrelated upto the lag time of 0.1ms (Figure S13C). Normalization of the ACF curves $[(G(t) - G(\infty))/(G(0) - G(\infty))]$ of nuclear and cytoplasmic compartments of anterior and posterior domains reveal differential mobility of Bcd::eGFP (Figure S13D). Further, we tested differential changes in dynamics of cytoplasmic bicoid at different location along the anterior-posterior axis of the embryo at n.c.13 (Figure S13E and S13F). We noticed that the correlation amplitude (G(0)) drops down as we go down the concentration gradient, suggesting the signal become very low towards the posterior most (Figure S13E) and normalized data with 2-P fit (Figure S13F) reveal the changes in bicoid dynamics along the A-P axis.

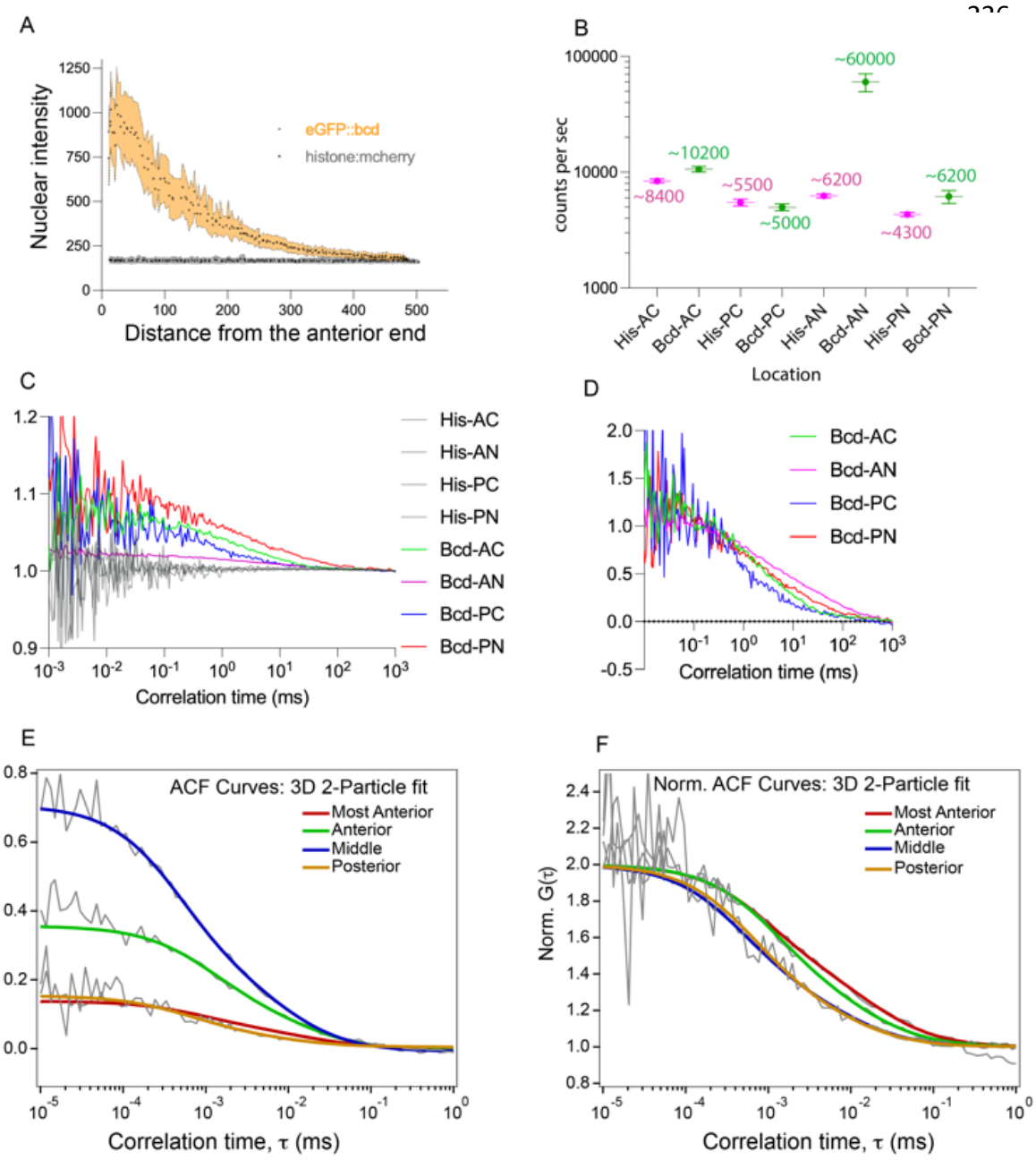


**Fig. S13 (related to Figs. 1,2 and S1). Determination of Background noise and spatial variation in eGFP::Bcd diffusion in the early embryo**

(A)Nuclear gradient profile of eGFP::Bicoid (orange) and histone mcherry (grey) from the anterior end of the blastoderm at n.c.14. (B) Photon counts per second measured from the n.c.14 embryos of eGFP::Bicoid (Green) and histone mcherry (magenta) from the cytoplasmic and nuclear compartments of anterior and posterior location. (C) ACF curves of Histone-mcherry (grey) compared to eGFP:Bicoid. Note the uncorrelated background noise from Histone-mcherry embryos. (D) Normalized ACF curves of eGFP:Bicoid from (C). (E) ACF curves (grey) and 3D 2-Particle fits without considering triplet state (colored) from 0.0001 ms to 1s from the cytoplasm measurements taken from equally distant location from the embryo's anterior end at early n.c. 13. Note the drop in the amplitude from the ACF curves of posterior most domain. (F) Normalized ACF curves from E.

**Details on SPIM based Imaging-FCS**

The setup included an illumination and detection arm placed orthogonal to each other. A 488 nm diode laser line (Cobolt 06-MLD 488nm 0488-06-01-0100-100, Cobolt AB, Sweden) was used to excite eGFP. The laser beam was directed through an optical fibre (kineFLEXP-3-S-405..640-1.0-4.0-P2, Qioptiq, United States) into the illumination arm consisting of an achromatic cylindrical lens ($f$ =75 mm; ACY254-075-A; Thorlabs Inc., United States) and an illumination objective (SLMPLN 20 × /0.25 NA; Olympus, Japan). The optical fibre expanded the beam sufficiently to overfill the back aperture of the illumination objective, and the cylindrical lens-objective pair was used to generate a static diffraction-limited light sheet.

On the detection arm, a detection objective (LUMPLFLN 60×/1.0 NA; Olympus, Japan) was housed in a custom-built sample chamber of dimensions 3 cm x 3 cm x 3 cm with a coverslip facing the illumination objective side and an opening on top for mounting the sample. The detection objective was coupled with a piezo flexure objective scanner (P-721 PIFOC; Physik Instruments, Germany) for fine control of the position of the detection objective with respect to the light sheet while focusing (100 nm step size). The signal captured by the objective was passed through a filter (FF03-510/20-25 Semrock, United States) to capture only the eGFP's fluorescence signal. The signal was then focused onto an EMCCD camera (Andor iXon3 860, 128 × 128 pixels; Andor Technology, United Kingdom) by a tube lens (LU074700, $f$ = 180 mm, Olympus, Japan). The illumination and detection arms were aligned to ensure that the light sheet coincided with the focal plane of the detection objective and that the signal from the thinnest section of the light sheet was captured at the centre of the camera.

eGFP::Bcd embryos were mounted in a Fluorinated Ethylene Propylene (FEP) tube of 1.1 × 1.5 $mm^2$ cross-section (FT 1.1 × 1.5, Adtech Polymer Engineering, England, United Kingdom) filled with 1% agarose (UltraPureTM Low Melting Point Agarose, 16520100, Thermofisher Scientific, United States) and positioned in a way that the anterior tip pointed into one of the walls of the tube. The FEP tube was held by self-closing forceps and mounted on a motorised stage with three linear positioning systems (Q-545 Q-MotionR Precision Linear Stage; Physik Instruments, Germany) with piezo motors for the three-axis and one rotation stage (DT-34 Miniature Rotation Stage; Physik Instruments, Germany). The FEP tube was placed in the sample chamber filled with water, and the tube was rotated to orient the anterior tip of the embryo to point towards the illumination objective to image the anterior margin with minimal illumination signal losses.

Since the position of the light sheet is fixed with respect to the detection objective, the embryo was imaged by moving the sample tube relative to the light sheet. The embryo was positioned such that the signal from the anterior margin was captured by the central region of the camera. This ensured that the

thinnest section of the light sheet illuminated this embryo region. A laser intensity of 30 W/cm$^2$ was used to illuminate the embryo for Imaging-FCS measurements.

For the Imaging FCS results in Figure S3, a time series image stack with 200,000 frames was recorded with an exposure time of 1 ms. The measurement was done in n.c. 13 to capture sufficient cytoplasm space. Since the nuclei moved during the measurement, only the first 80,000 frames were used to ensure that the nuclei stayed within the chosen ROI.

The image stack was analysed using an ImageJ plugin Imaging FCS 1.52 (Sankaran et al., 2021). Polynomial order 6 bleach correction was used. The fitting model used was:

$$G(\tau) = \frac{1}{N}\frac{g(\tau)}{g(0)}$$

where,

$$g(\tau) = \left\{\frac{\sqrt{4D\tau + \omega_{xy}^2}}{\sqrt{\pi}\cdot a} \times \left[e^{\left(-\frac{a^2}{4D\tau+\omega_{xy}^2}\right)} - 1\right] + \mathrm{erf}\left(\frac{a}{\sqrt{4D\tau + \omega_{xy}^2}}\right)\right\}^2 \times \left(1 + \frac{4D\tau}{\omega_Z^2}\right)^{-\frac{1}{2}} + G_\infty$$

where $a$ is the pixel size, $\tau$ is the lag time, $N$ is the number of particles, $D$ is the diffusion coefficient, $\omega_{xy}$ is the 1/e$^2$ radius of the PSF in the $xy$ direction, and $\omega_z$ is the 1/e$^2$ radius of the thickness of the light sheet. The value for the pixel size used for fitting was 400 nm, the value $\omega_{xy}$ used was 721 nm, and the value of $\omega_z$ was 1.13 µm and the fit parameters of D and N were recorded for every pixel to create the spatial D and the N maps.

## Additional Model Details

Models were solved in Matlab. Parameter optimisation was done using *fminsearch*. For each model, we performed 100 parameter minimisations, where we randomly sampled the experimental profile each time to generate distinct profiles (all within experimental error). Fitting was done by minimising the least square error. This was done both on the data values (which tended to more heavily weigh larger values, nearer the anterior) and on the logarithm of the data values (which tended to more heavily weigh smaller values, nearer the posterior). Both techniques gave similar results for the parameters, though the former better fit the profile in the anterior and the latter in the posterior.

### Model 1: SDD model

First, we considered the standard SDD model, with point source at $x = 0$.

$$\frac{\partial \rho(x,t)}{\partial t} = D\frac{\partial^2 \rho(x,t)}{dx^2} - \mu\rho \quad [1]$$

with boundary constraints

$$D\frac{\partial \rho(x=0,t)}{dx} + J = 0, \frac{\partial \rho(x=L,t)}{\partial x} = 0$$

But we need to account for folding of Bicoid at rate $\nu$:

$\rho_{total}(x,t) = \rho_{unfolded}(x,t) + \rho_{folded}(x,t)$, where

$$\frac{\partial \rho_u(x,t)}{\partial t} = D\frac{\partial^2 \rho_u(x,t)}{dx^2} - (\mu+\nu)\rho_u(x,t) \quad [2]$$

$$\frac{\partial \rho_f(x,t)}{\partial t} = D\frac{\partial^2 \rho_f(x,t)}{dx^2} + \nu\rho_u(x,t) - \mu\rho_f(x,t) \quad [3]$$

with boundary constraints

$$D\frac{\partial \rho_u(x=0,t)}{dx} + J = 0, \frac{\partial \rho_u(x=L,t)}{\partial x} = 0, \frac{\partial \rho_f(x=0,t)}{dx} = 0, \frac{\partial \rho_f(x=L,t)}{\partial x} = 0$$

This model is shown in Figure 2C.

### Model 2: SDD model with distributed source

We can adapt Model 1 to include an extended source. For simplicity, we define the source as $J$ if $x<x_0$ and zero otherwise. $x_0$ is left as a fitting parameter in the simulations.

The equations are as Model 1, except now equation [2] becomes

$$\frac{\partial \rho_u(x,t)}{\partial t} = D\frac{\partial^2 \rho_u(x,t)}{dx^2} - (\mu+\nu)\rho_u(x,t) + J \text{ if } x < x_0 \quad [4]$$

and $\frac{\partial \rho_u(x,t)}{\partial t} = D\frac{\partial^2 \rho_u(x,t)}{dx^2} - (\mu+\nu)\rho_u(x,t)$ if $x \geq x_0$

with boundary condition $\frac{\partial \rho_u(x=0,t)}{dx} = 0$

**Model 3: Two component model with no spatial variation**

We next consider a two-component model, where the diffusion coefficients do not vary across the embryo. We assume that Bicoid is in the fast form immediately after translation. We denote the two Bcd species by 1 and 2, denoting fast and slow forms respectively. We include a source domain region defined by $x_0$. The switching rate between fast and slow forms (denoted by α and β) are fitted constants, that do not vary across the embryo.

$$\frac{\partial \rho_{u,1}(x,t)}{\partial t} = D_1 \frac{\partial^2 \rho_{u,1}(x,t)}{dx^2} - (\mu + \nu + \beta)\rho_{u,1}(x,t) + \alpha\rho_{u,2}(x,t) + J \text{ if } x < x_0$$
$$\frac{\partial \rho_{u,1}(x,t)}{\partial t} = D_1 \frac{\partial^2 \rho_{u,1}(x,t)}{dx^2} - (\mu + \nu + \beta)\rho_{u,1}(x,t) + \alpha\rho_{u,2}(x,t) \quad \text{if } x \geq x_0 \qquad [5]$$

$$\frac{\partial f_{f,1}(x,t)}{\partial t} = D_1 \frac{\partial^2 \rho_{f,1}(x,t)}{dx^2} - (\mu + \beta)\rho_{f,1}(x,t) + \nu\rho_{u,1}(x,t) + \alpha\rho_{f,2}(x,t)$$

$$\frac{\partial \rho_{u,2}(x,t)}{\partial t} = D_2 \frac{\partial^2 \rho_{u,2}(x,t)}{dx^2} - (\mu + \nu + \alpha)\rho_{u,2}(x,t) + \beta\rho_{u,1}(x,t)$$

$$\frac{\partial \rho_{f,2}(x,t)}{\partial t} = D_2 \frac{\partial^2 \rho_{f,2}(x,t)}{dx^2} - (\mu + \alpha)\rho_{f,2}(x,t) + \beta\rho_{f,1}(x,t)$$

**Model 4: Two component model with spatial variation only in diffusion**

This version is as Model 3, except the first term on RHS is adapted to $\frac{\partial}{\partial x}\left(D_s(x)\frac{\partial}{\partial x}\rho_s(x,t)\right)$ where we take

$$D_s(x) = D_s(anterior) + (D_s(posterior) - D_s(anterior))\frac{x}{L} \qquad [6]$$

so that $D_s(0) = D_s(anterior)$ and $D_s(L) = D_s(posterior)$. This is a simple approximation to introduce spatially varying diffusion coefficients. Here, $L$ denotes the length along the AP axis, typically taken to be 500μm.

**Model 5: Two component model with spatial variation in diffusion and *β*** Same as Model 4, except now

$$\beta(x) = \beta_0 \cdot \left(1 + \right) \qquad \frac{x}{x+x_1} \qquad [7]$$

so $x_1$ is an additional fitting parameter. This is shown in Figure 3.

## Supplementary References


**Abu-Arish, A., Porcher, A., Czerwonka, A., Dostatni, N. and Fradin, C.** (2010). High mobility of bicoid captured by fluorescence correlation spectroscopy: implication for the rapid establishment of its gradient. *Biophys J* **99**, L33-35.

**Haupts, U., Maiti, S., Schwille, P. and Webb, W. W.** (1998). Dynamics of fluorescence fluctuations in green fluorescent protein observed by fluorescence correlation spectroscopy. *Proc Natl Acad Sci U S A* **95**, 13573-13578.

**Jimenez-Banzo, A., Nonell, S., Hofkens, J. and Flors, C.** (2008). Singlet oxygen photosensitization by EGFP and its chromophore HBDI. *Biophys J* **94**, 168-172.

**Kapusta, P.** (2010). Absolute Diffusion Coefficients:Compilation of Reference Data for FCS Calibration. *PicoQuant*.

**Sankaran, J., Balasubramanian, H., Tang, W. H., Ng, X. W., Rollin, A. and Wohland, T.** (2021). Simultaneous spatiotemporal super-resolution and multi-parametric fluorescence microscopy. *Nat Commun* **12**, 1748.

**Widengren, J., Mets, Ü. and Rigler, R.** (1999). Photodynamic properties of green fluorescent proteins investigated by fluorescence correlation spectroscopy. *Chemical Physics* **250**, 171-186.